NTNU

Norwegian University of
Science and Technology

Molecular dynamics simulation of sodium diffusion in amorphous carbon using optimized reactive force field

Anh Quynh Nguyen

Chemistry
Submission date: May 2017
Supervisor: Henrik Koch, IKJ
Co-supervisor: Eirik Hjertenæs, IKJ

Norwegian University of Science and Technology
Department of Chemistry

Abstract

A reactive force field has been developed to study sodium intercalation and diffusion into graphitic carbon at high temperature. The resulting force field reproduces training data and calculates new data with moderate accuracy. It has been applied in computer simulations of atomistic models representing sodium diffusion in graphitic carbon. In this thesis, the force field is further employed to simulate sodium intrusion in generated amorphous models at room temperature. The goal is to qualitatively evaluate the ability of the force field to describe sodium interaction in relevant carbon structures at lower temperature.

Amorphous carbon models have been generated by the liquid-quench routine. The radial distribution functions of these amorphous structures give a good fit to the experimental data. The successive peaks shows that the structures contain largely of sp^2 hybridized bonds, suggesting the carbon atoms are fused in rings. Results from the computed angle distribution functions reveal that the structures are mostly comprised of six-membered rings, with small amount of five- and seven-membered rings. Sodium atoms of two different densities are subsequently inserted into the amorphous structures. For the case of low density, sodium atoms enter the structures through the insertion sites of low energy, occupying these sites and preventing further insertion. At higher density, the sodium atoms exert a higher pressure on the carbon structure. More sodium atoms are able to enter the structure through insertion sites of higher energy. These simulation results demonstrate that the force field is able to qualitatively describe sodium diffusion into amorphous carbon.

Sammendrag

Natrium ionbatteri (NIB) er et billigere alternativ til det populære litium ionbatteri (LIB) som oppladbare ionbatteri. NIB er fortsatt i en tidlig forskingsfase, og så langt mangler det fortsatt et anodemateriale som interkalerer natrium effektivt nok. Grafittanoder brukt i LIB er dessverre uegnet. Amorf karbon som et porøst material har derimot flere innsettingsposisjoner og dermed vist høyere diffusjon kapasitet. I denne oppgaven blir natrium diffusjon i amorf karbonstruktur undersøkt på atomnivå med en teoretisk beregningsmetode basert på kvantekjemi.

Et empirisk reaktivt kraftfelt (ReaxFF) har blitt laget for å studere natriuminntrenging i grafittisk karbon ved høy temperatur. Det resulterende kraftfeltet har reprodusert treningsdata og utført nye beregninger med en kvalitativ akseptabel nøyaktighet. Videre har kraftfeltet også blitt brukt til å modellere natrium adsorpsjon på primitiv og defekte grafittstruktur. Dette kraftfeltet er nå brukt til å simulere natrium diffusjon i amorf karbonstruktur ved romtemperatur. På denne måten blir kraftfeltet testet i å beregne en helt annen karbonstruktur og utføre simulering ved romtemperatur.

Ved hjelp av liquid-quench metoden blir flere amorf karbonstrukturer generert. Radial distribusjonsfunksjoner (RDF) av disse viser sammenlignbare trekk med litteraturverdier. RDF indikerer at karbonstrukturene inneholder mest sp^2 hybridisert karbon, og kun en liten del av sp^3, noe som tyder på at karbonatomer er fusjonert i ringer. Resultatene fra vinkel distribusjonsfunksjonen bekrefter at strukturene består stort sett av seksringer med en liten av fem- og syvringer. To strukturer blir brukt videre for innsetting av forholdsvis 21 og 41 Na atomer. I det første tilfelle koloniserer natrium innsettingssidene med lavest energi og blokkerer for videre innsetting. Når antall Na atomer økes, går flere natriumatomer inn i strukturen og utvide karboncellen på grunn av det høye trykke fra Na atomer. Disse resultatene viser at kraftfeltet er i stand til å produsere ikke-grafittiske karbon system og beskrive natriuminnsetting med kvalitativ god nøyaktighet.

Preface

The master thesis has been submitted at the Department of Chemistry, Norwegian University of Science and Technology (NTNU) in Trondheim.

First and foremost, I want to express my gratitude to my supervisor, professor Henrik Koch for his guidance and patience during the thesis work, and to his former PhD student Eirik Hjertenæs for the opportunity to participate in developing the force field. It has been very interesting and informative to work with both of you.

I would like to thank my classmates for the best five years at NTNU. I cherish all the good memories from our trip to Asia, one-hour lunch and coffee breaks, writing long reports and atom packing jokes. NTNU would have not been the same without you.

A special thanks to Jakob Wuttudal for his admirable patience and encouragement every day through this journey. Always listening to my complains, helping me through my struggles, and best of all making me smile. Many thanks to him and Raffaela Cabriolu for proofreading the thesis, and for their suggestions and advice.

Last but certainly not least, I want to thank my parents and grandparents for always pushing me to do my best, I owe my success to you. Your endless love and support have made me the person I am today. A special memory to my grandmother, who passed away in this time.

Contents

Abbreviations

a-C Amorphous carbon
BO Born-Oppenheimer approximation
CI Configuration interaction
DFT Density functional theory
DLC Diamond-like carbon
EEM Electronegativity equalization method
EES Electric energy storage
FF Force field
HF Hartree-Fock
GGA Generalized Gradient Approximation
LDA Local density approximation
LIB Lithium ion battery
MD Molecular dynamics simulation
MDC-q Multipole Derived Charges up to Quadrupole Moment
MO Molecular orbital
MM Molecular Mechanics method
NIB Sodium ion battery
PBE Perdew-Burke-Ernzerhof functional
RDF Radial distribution function
ReaxFF Reactive force field
RHF Restricted closed-shell Hartree-Fock
SCF Self-consistent field
SD Slater determinant
SE Schrödinger equation
QEq Charge Equilibration method
QM Quantum mechanics

Chapter 1

Introduction

Technological advances in producing renewable energy sources have encouraged and laid foundation for research in large-scale energy storage systems (EES) [1, 2]. Among storage methods, electrochemical energy storage has received considerable attention with particularly rechargeable ion-batteries in mind. Commercialized first in 1991, lithium-ion batteries (LIBs) have grown immensely in the secondary battery market and completely replaced nickel batteries. Due to their high energy density, long cycle life and safety, LIBs are the most popular choice for energy storage in portable electronic products. However, large-scale application of LIBs suffers from limited availability of lithium sources resulting in high cost. Alternatives have been suggested, in which sodium-ion batteries (NIBs) have emerged to be the most promising substitute to LIBs.

Sodium, the next alkali metal after Li, shares similar chemical properties and has shown comparable electrochemical properties to Li. More importantly, sodium is abundantly distributed and has unlimited resources, attracting more attention to NIBs as a low-cost alternative to LIBs. Although great advances have been made in research and development of NIBs, several challenges still remain, especially for the negative electrode. Graphite, the conventional anode in LIBs, fails to intercalate appreciable amounts of sodium ions, as the larger ionic radius of sodium prevents rapid diffusion into graphite layers. Non-graphitic carbons containing graphite-like layers and micropores, however, have shown high electrochemical activity and reversible capacity. Highly disordered amorphous carbons have also drawn great deal of attention. Through an *ab initio* computational-experimental study, Legrain *et al.* has demonstrated that amorphization of carbon actually enhances and favors sodium insertion [3]. They studied carbon systems of only 64 atoms due to the high computational cost of *ab initio* approach. Motivated by this, an empirical potential is used to generate a larger amorphous carbon (a-C) model and subsequently simulate sodium insertion into the resulted structure.

Molecular dynamics (MD) simulations have become essential in studying dynamic details of novel systems. Interactions between atoms can be computed using either quantum mechanics (QM) or empirical force field (FF) methods, where the former provides high accuracy accompanied with a computational cost, limiting their use to smaller model systems. To be able to simulate larger model systems and as the same time retain high accuracy, one must resort to empirical approaches. Reactive force field (ReaxFF) simulations have shown to accurately describe chemical reactivity using the bond-order formalism. Chemical bond breaking and forming are simulated, and non-bonded interactions are calculated between all atoms. $\text{ReaxFF}_{\text{LiC}}$ has

been formerly developed to study lithium intercalation in LIBs on the atomic scale. With a similar purpose, $\text{ReaxFF}_{\text{NaC}}$ is developed to describe sodium interaction in graphitic carbon, as the process plays an important role in cathode wear in aluminum electrolysis [4]. The force field has been parametrized against a training set of *ab initio* derived data. It reproduces training data with reasonably accuracy and exhibit satisfactory predictive power. The details of the optimization process in developing the force field will be described in details.

The optimized force field has been applied to simulate sodium intercalation in graphitic carbon related to aluminium electrolysis. In this thesis, the same force field is used to simulate sodium diffusion in generated amorphous carbon models. This sodium uptake is studied in connection to field of ion-battery. An important distinction between these applications is the operational temperature. Ion batteries operate at ambient temperatures while carbon cathodes are used at temperatures close to 1000°C. In addition, there are structurally differences between graphitic and amorphous carbon. The latter consists of sp^2 and sp^3 hybridized bonds and dangling bond, exhibiting different structural features and insertion sites for sodium. In graphite sodium atoms intercalate between the layers, whereas they accommodate voids, micro- and micropores within the amorphous structure, presenting a different diffusion mechanism. As Reax_{NaC} is parametrized to study sodium diffusion in graphitic carbon at high temperature,it can yield unexpected results and might be inadequate in this case.

1.0.1 Scope of this work

The optimized force field $\text{ReaxFF}_{\text{NaC}}$ is being employed to generate amorphous carbon models and simulated sodium insertion into these at room temperature. Molecular dynamics simulations is performed in the canonical ensemble with a Nose-Hoover thermostat (NVT), carefully controlling the rapidly change in temperature, and at the same time preserving the correct thermodynamics.

Amorphous carbon models are generated by rapid quenching of liquid carbon to room temperature. All simulated systems are quenched linearly with a quenching rate below a certain threshold to avoid structural defects and forming a more appropriate amorphous structure [5]. The density value is chosen to be the same as that of Legrain [3] to compare the results. The initial configuration is created by randomly distributing the carbon atoms in the simulation cell. Because of this, various carbon structures can be obtained with different structural features. Several structures are therefore sampled, for which the radial distribution functions (RDF) are compared to the experimental RDF by Gilkes [6]. Those structures that give a good fit of the RDF to the experimental have been exposed to sodium insertion at room temperature. Two different densities of sodium have been studied. The RDF and the angle distribution function are used to give an insight of the atomistic structure of the sodium inserted amorphous structures.

Chapter 2

Fundamentals of computational chemistry

This chapter briefly introduces the theoretical basis of computational chemistry. Majority of the theory and the notation can be found in *Modern Quantum Chemistry* by Szabo and Ostlund [7]. The section about density functional theory is drawn from *Molecular Quantum Mechanics* by Atkins and Friedman [8]. Sections and equations found elsewhere are referred explicitly. Atomic units are used throughout to simplify the notation.

2.1 Introduction

Computational chemistry is a field of chemistry that uses computers to perform calculations based on a given theoretical method. It has become an indispensable tool in research, providing valuable information about chemical systems that otherwise are difficult or impossible to obtain with experiments. Today, computational techniques are routinely used in parallel with experiments in order to explain and verify experimental observations. Several powerful molecular modelling tools have been developed. They are able to accurately predict structures, energies and other properties of molecules, dealing with thousands of atoms. The rapid advancements in computational chemistry are largely due to the improvement in computer resources, allowing simulations to be performed efficiently. It is important though, to emphasize that computational chemistry does not replace for experimental studies, but assist in comparing experimental/computational results and exploring new chemistry.

The success of modelling methods rests upon the theoretical description of the atoms and their interactions. Many theoretical formulations have been established, ranging from very approximate to highly accurate. Quantum mechanical (QM) methods offer high accuracy, but can be quite expensive in terms of computer resources required. Quantum mechanics comprises of the most fundamental methods in computational chemistry that attempt to solve the electronic structure of a system. Methods within this field of electronic structure theory can be classified either as *wavefunction* based or *density functional* based. In the former class, the methods are dedicated to find an approximation of the electronic wavefunction as a solution to the

Schrödinger equation. In density functional theory (DFT), the electronic energy is considered as an energy functional of the electron density. Moreover, it is important to distinguish between *ab initio* and semi-empirical methods. The term *ab initio* or "from first principle "involves methods that are solely based on theoretical principles, without any empirical parameters. Semi-empirical methods employ empirical parameters to the approximations, mainly to simplify the extensive *ab initio* calculation and reduce computation time. Most wavefunction based methods are *ab initio*, whereas DFT falls in between these two classes as some DFT-based approaches contain empirical parameters.

All computational methods aim to be universally accurate and offer reasonable scaling with the system size. In practice, there exists a trade-off between the obtained level of accuracy and computational cost. The term *accuracy* represents a combined measure of the quality and reliability of the calculated/predicted result. *Ab initio* methods provides high accuracy accompanied with a high computational cost, and are generally limited to small system size. On the other hand, the more approximate molecular mechanic (MM) approaches, also known as empirical force (FF), are computationally less demanding and display a modest scaling with the system size. Force field methods calculate the potential energy from a parametric function. The parameters can be tuned and fitted to experimental or *ab initio* derived data. Although force field methods are more approximated, it does not necessarily mean that these methods are less accurate. In some case, force field can provide results with comparable accuracy as high-level QM methods. Molecular mechanics is discussed in the next chapter.

2.2 The electronic problem

The main objective of electronic structure theory is finding approximate solutions to the time-independent Schrödinger equation (SE):

$$\hat{H}|\Psi\rangle = E|\Psi\rangle, \tag{2.1}$$

where $\hat{H}$ is the Hamiltonian operator, and the wavefunction Ψ is a set of solutions, or eigenstates, of the Hamiltonian. Associated with each solution, Ψ_n, is an energy eigenvalue, E_n, that satisfies the Schrödinger eigenvalue equation. For a system with N electrons and M nuclei, the Hamiltonian is written as:

$$\hat{H} = -\frac{1}{2}\sum_{i=1}^{N}\nabla_i^2 - \sum_{I=1}^{M}\frac{1}{2M_I}\nabla_I^2 - \sum_{i=1}^{N}\sum_{I=1}^{M}\frac{Z_I}{r_{i,I}} + \sum_{i=1,j>i}^{N}\frac{1}{r_{ij}} + \sum_{I,J=1}^{M}\frac{Z_I Z_J}{r_{IJ}}. \tag{2.2}$$

The capital indices I, J denote the nuclei, and lower cases i, j denote the electrons. The quantity Z is the nuclear charge, M the nuclear mass and r is the position vector. The five operators in the equation above represents the kinetic energy of the electrons, the kinetic energy of the nuclei, the coulomb attraction between electrons and nuclei, and the repulsion between electrons and between nuclei, respectively. Eq. 2.2 seems deceptively simple by its form, but it is extremely complex to solve. For any systems with more than two electrons the SE becomes intractable and cannot be solved exactly. Thus, reasonable approximations have to be made to reduce the complexity of the problem. The first indispensable approximation that decouples the motions of the electrons and nuclei is the Born-Oppenheimer approximation.

2.2.1 The Born-Oppenheimer approximation

For many-electron molecular systems, the total wavefunction and its Hamiltonian are extremely difficult to express. To simplify this problem somewhat, the Born-Oppenheimer approximation (BO) can be applied. Based on the fact that the nuclei are much heavier than the electrons, they move much more slowly. As such, the electrons can be considered to be moving in the field of fixed nuclei. The molecular wavefunction can then be written as a product of a nuclear, Ψ_{nuc}, and an electronic, Ψ_{el}, wavefunction:

$$\Psi(\mathbf{r}, \mathbf{R}) = \Psi_{\text{nuc}}(\mathbf{R})\Psi_{\text{el}}(\mathbf{r}; \mathbf{R}), \tag{2.3}$$

where Ψ_{el} is a function of the electronic coordinates $\mathbf{r}$, and only depends parametrically on the nuclear positions $\mathbf{R}$. Moreover, the kinetic energy for the nuclei in Eq. 2.2 can be neglected, and the repulsion between the nuclei considered to be constant, yielding the electronic Hamiltonian, $\hat{H}_{\text{el}}$, of the form:

$$\hat{H}_{\text{el}} = -\frac{1}{2}\sum_{i=1}^{N}\nabla_i^2 - \sum_{i=1}^{N}\sum_{I=1}^{M}\frac{Z_I}{r_{i,I}} + \sum_{i=1,j>i}^{N}\frac{1}{r_{ij}}. \tag{2.4}$$

The electronic wavefunction is the solution to the electronic Schrödinger equation:

$$\hat{H}_{\text{el}}\Psi_{\text{el}}(\boldsymbol{r}; \boldsymbol{R}) = E_{\text{el}}(\boldsymbol{R})\Psi_{\text{el}}(\mathbf{r}; \mathbf{R}), \tag{2.5}$$

where the electronic energy E_{el} also depends parametrically on the nuclear coordinates. By solving the electronic SE for all possible nuclear positions, a potential energy surface (PES) is generated, on which the nuclei move along. The minimum of the potential curve corresponds to the equilibrium configuration of the nuclei.

Adopting the BO approximation simplifies the quantum problem to solving the electronic problem Eq. 2.5. Although the complexity is reduced, the electronic SE still depends on $3N$ coordinates, and only approximations can be found. Approximations can be deduced either in the wavefunction and/or in the Hamiltonian operator.

2.2.2 The variational principle

Another important theorem in finding approximate solutions to the Schrödinger equation is the variational principle. It states that for any arbitrary trial wavefunction, $|\tilde{\Psi}\rangle$, the expectation value of the electronic Hamiltonian is always larger than the electronic ground state energy E_0:

$$\tilde{E}_i \geq E_0, \tag{2.6}$$

where the equality sign only holds when $|\tilde{\Psi}\rangle = |\Psi_0\rangle$. The expectation value $\tilde{E}_i$ is defined as the Rayleigh ratio [8]:

$$\tilde{E}_i = \frac{\langle\tilde{\Psi}_i|\hat{H}|\tilde{\Psi}_i\rangle}{\langle\tilde{\Psi}_i|\tilde{\Psi}_i\rangle}. \tag{2.7}$$

The wavefunction that gives the lowest ratio is the best approximate wavefunction. The Rayleigh ratio thus measures the quality of the trial wavefunction and serves as an upper bound to the true ground state energy.

Given a wavefunction that depends on certain parameters, these parameters can be adjusted and varied until the expectation value reaches the minimum. The obtained minimum value is a variational estimate of the exact ground state energy.

2.2.3 Molecular orbital and Slater determinant

To completely describe a single electron, its spin must be specified. An appropriate one-electron wavefunction that describes both the spatial coordinates and spin is the spin orbital, $\chi_i(\boldsymbol{x})$, which is a product of a spatial orbital $\psi_i(\boldsymbol{r})$ and a spin function $\sigma_i(\omega)$:

$$\chi_i(\boldsymbol{x}) \equiv \psi_i(\boldsymbol{r})\sigma_i(\omega), \tag{2.8}$$

where $\sigma_i = \alpha$ or β corresponding to spin up and spin down. The spin orbitals are orthonormal and depend on four variables denoted by $\boldsymbol{x} = \{\boldsymbol{r}, \omega\}$.

As electrons are indistinguishable, exchanging any pair of electrons does not effect the distribution of the electron density, i.e. $|\Psi|^2$ is invariant. This implies that the wavefunction must change sign when the spatial and spin coordinates $\boldsymbol{x}$ are interchanged. More specific, the many-electron wavefunction must be antisymmetric with respect to the interchange of any two electrons:

$$\Psi(\boldsymbol{x}_1, ..., \boldsymbol{x}_i, ..., \boldsymbol{x}_j, ..., \boldsymbol{x}_N) = -\Psi(\boldsymbol{x}_1, ..., \boldsymbol{x}_j, ..., \boldsymbol{x}_i, ..., \boldsymbol{x}_N). \tag{2.9}$$

The requirement is known as the *antisymmetry principle*, which is equivalent to the Pauli exclusion principle requiring that no more than one electron can occupy a spin orbital. Consequently, the exact wavefunction must satisfy the Schrödinger equation and the antisymmetry principle.

For a system of N non-interacting electrons, the wavefunction can be intuitively written as the product of individual spin orbitals for each electron:

$$\Psi^{\mathrm{HP}}(\boldsymbol{x}_1, \cdots, \boldsymbol{x}_N) = \chi_i(\boldsymbol{x}_1)\chi_j(\boldsymbol{x}_2)\cdots\chi_k(\boldsymbol{x}_N). \tag{2.10}$$

This is the *Hartree product* wavefunction, in which the energy eigenvalue is the sum of the one-electron energy eigenvalues. The square of the Hartree wavefunction becomes

$$|\Psi^{\mathrm{HP}}(\boldsymbol{x}_1, \cdots, \boldsymbol{x}_N)|^2 d\boldsymbol{x}_1 \cdots d\boldsymbol{x}_N = |\chi_i(\boldsymbol{x}_1)|^2 d\boldsymbol{x}_1 \cdots |\chi_k(\boldsymbol{x}_N)|^2 d\boldsymbol{x}_N, \tag{2.11}$$

which indicates that the probability of finding one particular electron at a given point of space is independent of the positions of neighboring electrons. This is not fundamentally correct. In reality, the motion of electrons are explicitly correlated. Electrons repel each other and tend to avoid the region of space occupied by other electrons. When considering independent electrons, the Hartree product also does not take into account the indistinguishability of electrons, i.e. it does not satisfy the antisymmetric requirement stated above.

To ensure the antisymmetry principle, the wavefunction can be written as a Slater determinant (SD), where all possible linear combinations of the Hartree products are included. For a fully interacting N-electron

system the Slater determinant is expressed as:

$$\Psi(\boldsymbol{x}_1, ..., \boldsymbol{x}_N) = \frac{1}{\sqrt{N!}} \begin{vmatrix} \chi_i(\boldsymbol{x}_1) & \chi_j(\boldsymbol{x}_1) & \cdots & \chi_k(\boldsymbol{x}_1) \\ \chi_i(\boldsymbol{x}_2) & \chi_j(\boldsymbol{x}_2) & \cdots & \chi_k(\boldsymbol{x}_2) \\ \vdots & \vdots & & \vdots \\ \chi_i(\boldsymbol{x}_N) & \chi_j(\boldsymbol{x}_N) & \cdots & \chi_k(\boldsymbol{x}_N) \end{vmatrix}, \tag{2.12}$$

where $(N!)^{-1/2}$ is a normalization factor. The rows are labeled by electrons while the columns by spin orbitals. Interchanging two rows of the SD, which corresponds to changing the coordinates of two electrons, changes the sign of the SD. Two electrons occupying the same spin orbital is the same as having two equal columns, making the SD zero.

2.3 Wavefunction-based methods

Wavefunction based methods are dedicated to explicitly finding approximate solutions to the electronic Schrödinger equation through the wavefunction. The simplest wavefunction-based, yet the most fundamental method is the Hartree-Fock. It forms the foundation for more elaborate and advanced electronic structure methods. Post-HF methods are subsequently developed to incorporate the electron correlation that the HF fails to describe in its wavefunction. Among these methods one can find the configuration interaction (CI), the coupled cluster (CC) and methods based on the many-body perturbation theory (MBPT) such as the second-order Møller–Plesset (MP2) method. The Hartree-Fock approach is described first, followed by the CI method to demonstrate the error in HF and how it can be corrected.

2.3.1 The Hartree-Fock method

The Hartree-Fock (HF) method is central in finding approximate solutions to the electronic Schrödinger equation. It is regarded as a starting point for advanced *ab initio* methods. The HF approximation is equivalent to the molecular orbital (MO) approximation describing electrons occupying orbitals.

The single Slater determinant formed from a set of spin orbitals $\{\chi_a\}$ is the best approximation to the ground state wavefunction for an N-electron system:

$$|\Psi_0\rangle = |\chi_1\chi_2 \cdots \chi_a\chi_b \cdots \chi_N\rangle. \tag{2.13}$$

The electronic energy of the Slater determinant, or more precisely the expectation value of the electronic Hamiltonian, can be written as:

$$E_0 = \langle\Psi_0|\hat{H}|\Psi_0\rangle = \sum_i^N h_{ii} + \frac{1}{2}\sum_{i,j}^N (J_{ij} - K_{ij}). \tag{2.14}$$

The two summation terms are the one- and two-electron matrices, respectively. The former matrix contains one-electron elements describing the average kinetic and nuclear attraction of each electron:

$$h_{ii} = \langle\chi_i(\boldsymbol{x}_1)|\hat{h}(\boldsymbol{x}_1)|\chi_i(\boldsymbol{x}_1)\rangle, \tag{2.15}$$

where the core Hamiltonian $\hat{h}$ is

$$\hat{h}(i) = -\frac{1}{2}\nabla_i^2 - \sum_I \frac{Z_I}{r_{i,I}}. \tag{2.16}$$

The two-electron matrices, J and K, represent the expectation value of the coulomb and exchange operators, respectively. Each element in the coulomb matrix J describes the classical electrostatic repulsion between two electrons, one occupying orbital i and another orbital j, and can be written as:

$$J_{ij} = \langle ij|ij\rangle = \int d\boldsymbol{x}_1 d\boldsymbol{x}_2 \chi_i^*(\boldsymbol{x}_1)\chi_i(\boldsymbol{x}_1) r_{12}^{-1} \chi_j^*(\boldsymbol{x}_2)\chi_j(\boldsymbol{x}_2) \tag{2.17}$$

The exchange term K_{ij} arises from the antisymmetric nature of the Slater determinant and does not have a simple classical analog. Its elements are given by:

$$K_{ij} = \langle ij|ji\rangle = \int d\boldsymbol{x}_1 d\boldsymbol{x}_2 \chi_i^*(\boldsymbol{x}_1)\chi_j(\boldsymbol{x}_1) r_{12}^{-1} \chi_j^*(\boldsymbol{x}_2)\chi_i(\boldsymbol{x}_2). \tag{2.18}$$

According to the variational principle, the best approximate wavefunction is the one that yields the lowest possible energy given in Eq. 2.14. By minimizing the energy with respect to the spin orbitals and constraining that the spin orbitals remain orthonormal ($\langle\chi_i|\chi_j\rangle = \delta_{ij}$), it results in a set of independent integro-differential equations, known as the Hartree-Fock equations:

$$\hat{f}(\boldsymbol{x}_1)\chi_i(\boldsymbol{x}_1) = \varepsilon_i \chi_i(\boldsymbol{x}_1). \tag{2.19}$$

The HF equations are thus eigenvalue equations with the spin orbitals as eigenfunctions and spin orbital energy as eigenvalues. The effective one-electron Fock operator $\hat{f}(\boldsymbol{x}_1)$ is a sum of the core-Hamiltonian operator, $\hat{h}$, and the average potential operator $v^{\mathrm{HF}}(\boldsymbol{x}_1)$ comprising of the coulomb and exchange operators:

$$\hat{f}(\boldsymbol{x}_1) = \hat{h}(\boldsymbol{x}_1) + \underbrace{\sum_i^N \left(\hat{J}_i(\boldsymbol{x}_1) - \hat{K}_i(\boldsymbol{x}_1)\right)}_{v^{\mathrm{HF}}(\boldsymbol{x}_1)}. \tag{2.20}$$

The Hartree-Fock potential $v_{HF}(\boldsymbol{x}_1)$ is the average potential experienced by electron one, arising from the approximation that each electron moves within an average field due to the presence of the other $(N-1)$ electrons. As a result, the HF method simplifies the complicated many-electron problem to one-electron problem, in which the electron-electron repulsion is treated in an average way. The general strategy to solve the HF equations is called the self-consistent field (SCF) method. By guessing the initial spin orbitals, one can then calculate the average potential field. The eigenvalue equation is then solved to obtain a new set of spin orbitals, which are used in the next iteration. As follows, one can obtain new potential field for each set of spin orbitals and repeat the procedure until convergence is reached or when no further changes are observed in the potential field.

Further description of the Hartree-Fock approach is limited to a common variant of HF, namely restricted closed-shell Hartree-Fock (RHF). The method deals with an even number of N electrons, and all electrons are paired with opposite spin such that $(N/2)$ spatial orbitals are doubly occupied. The spin orbitals of both spin functions are thus restricted to have identical spatial orbitals, yielding the closed-shell ground state wavefunction:

$$|\Psi_0\rangle = |\psi_1\bar{\psi}_1 \cdots \psi_a\bar{\psi}_a \cdots \psi_{N/2}\bar{\psi}_{N/2}\rangle. \tag{2.21}$$

Integrating out the spin functions, Eq. 2.19 modifies to a spatial equation, with each spatial molecular orbital doubly occupied $\{\psi_a | a = 1, ..., N/2\}$. The closed-shell spatial eigenvalue equation becomes:

$$\hat{f}(\boldsymbol{r}_1)\psi_i = \varepsilon_i \psi_i(\boldsymbol{r}_1), \tag{2.22}$$

along with the closed-shell Fock operator

$$\hat{f}(\boldsymbol{r}_1) = \hat{h}(\boldsymbol{r}_1) + \sum_{j}^{N/2} 2J_j(\boldsymbol{r}_1) - K_j(\boldsymbol{r}_1). \tag{2.23}$$

Solving Eq. 2.22 is equivalent to calculating the MOs, $\psi_i(\boldsymbol{r}_1)$, which are unknown at this point. This has been solved by Roothaan, who introduces the concept of expanding the unknown molecular orbitals as a linear combination of known basis functions (atomic orbitals). Given a set of K known basis functions $\{\phi_\mu | \mu = 1, ..., K\}$, the unknown molecular orbitals are linearly expanding as:

$$\psi_i = \sum_{\mu=1}^{K} C_{\mu i}\phi_\mu, \qquad i = 1, ..., K, \tag{2.24}$$

where $C_{\mu i}$ are expansion coefficients. In practice, one is always limited to a finite set of K basis function due to computational reasons. A large basis set is able to describe the molecular orbitals more accurately, and thus the HF energy are lowering. As the set of basis functions essentially complete, the energy reaches a limit called the Hartree-Fock limit. For a finite basis set, the obtained energy is somewhat above this limit.

Expressing the MOs in terms of basis functions simplifies the calculation to determine the a set of expansion coefficient. To do so, the linear expansion of MOs is substituted into the HF equation, yielding matrix eigenvalue equations, also known as the Roothaan equations. Written in a more compact form, the single matrix equation is expressed as:

$$\mathbf{FC} = \mathbf{SC}\boldsymbol{\varepsilon}, \tag{2.25}$$

where $\boldsymbol{\varepsilon}$ is the diagonal matrix of the orbital energies. The Fock matrix $\mathbf{F}$ is the matrix representation of the one-electron Fock operators of the form Eq. 2.23 in the basis $\{\phi_\mu\}$. The matrix $\mathbf{C}$ contains the coefficients to be determined. The overlap matrix $\mathbf{S}$ defined as the overlap integral ($S_{ij} = \langle\phi_i|\phi_j\rangle$) ensures the orthonormality of the basis functions. The Roothaan equations can be solved using matrix algebra. They are nonlinear and must be solved iteratively in the SCF approach.

Basis set

The set of basis functions $\{\phi_\mu\}$ is commonly referred as the basis set. If the basis set is complete, the expansion for molecular orbitals in Eq. 2.24 is exact, known as the basis set limit. A complete basis set involves an infinite number of basis functions, which is impossible to handle in practice. One is always restricted to a finite basis set, accepting a certain basis set truncation error. Larger basis sets lead to more accurate molecular orbitals and hence lower energies, though at the same time raise the computational cost. It is therefore crucial to choose a basis set that provides a reasonably accurate description of molecular orbitals and has a low computational cost as possible.

There exists a large variety of basis set functions. In early quantum chemistry, Slater type orbitals (STOs) and Gaussian-type orbitals (GTOs) were the most popular basis functions. STOs are able to give excellent fit with the hydrogenic orbitals because of the exponential dependence on the distance. However, the calculation of the four-center two-electron integrals in SCF approach with STOs is very difficult and time-consuming. Thus, STOs are generally restricted to atomic and diatomic systems. On the contrary, the two-electron integrals are relatively easy to evaluate with GTOs. In practice, the STOs are often constructed from primitive Gaussian functions comprising of single basis functions. It involves using linear combination of primitive Gaussian functions, known as contracted GTOs, to mimic a STO. The most common basis set of this kind is the STO-3G basis set, where three GTOs are used to give the best fit to the corresponding STO.

A minimal basis set is the smallest basis set containing just enough basis functions to describes all electrons in the system. For most problems, the minimal basis set is not sufficient to give good results. To improve the basis set, the basis functions can be doubled and tripled, and so on, producing double zeta (DZ) and triple zeta (TZ) type basis. Further improvement to these basis set extensions is to add polarization or diffusion functions. The purpose of the former type is to improve the description of covalent bonds, while the latter is to correctly describe the electron charge distribution at large distances from the nuclei.

Adding more basis functions increases the accuracy of the basis set, and indeed also increases the computational cost. One way to bypass this is to enlarge the basis for the valence orbitals while keep the core orbitals in minimal basis, also known as split-valence basis set. For example, the basis set 6-21G is a double split valence set. The core orbitals are described by one contracted GTO comprised of six primitive GTOs, and a split of two contracted GTOs, one of three primitive GTOs and the other of one GTO to describe the valence orbitals.

Another type of basis set is the correlation consistent basis sets (cc) developed by Dunning and co-workers [9], with the purpose to recover the correlation energy of electrons. The cc-basis set are polarized X-zeta Gaussian basis functions expressed with the acronym cc-pVXZ (X = D, T , Q, 5, 6, 7), specially designed to include functions that contribute similar amounts of correlation energy at the same stage. For example, the contributions from $2d$ and $1f$ functions are similar, so they will be added at the same time. The cc-basis sets can also be augmented with an additional set of diffuse functions with a smaller exponent for each angular momentum present in the basis [10]. This is denoted with the prefix "aug". Extra core functions can also be added for accurately describing the electron distribution close to the nuclei. These are written with the acronym cc-pCVXZ.

2.3.2 Configuration interaction method

The most significant drawback of Hartree-Fock theory is that it ignores the electron correlation. As described above, the HF method considers each electron to be moving in an average potential field of all the other electrons, and neglects the fact that the electron motions are correlated. Using just a single Slater determinant, HF produces energy eigenvalues that are too high. To properly define the electron correlation, it is necessary to present the *ab initio* method configuration interaction (CI).

The HF method generates a finite set of $2K$ spin orbitals, $\{\chi_k\}$, when using a finite basis set expansion of K spatial functions. Ordering these spin orbitals according their energy, N orbitals with the lowest energies are

occupied with one electron each, whereas the remaining $(2K - N)$ are unoccupied or virtual spin orbitals. This gives a set of occupied spin orbitals, $\{\chi_a\}$, and a set of virtual spin orbitals $\{\chi_r\}$. The Slater determinant obtained from the occupied set $\{\chi_a\}$ is the variational Hartree-Fock ground state wavefunction, $|\Psi_0\rangle$:

$$|\Psi_0\rangle = |\chi_1\chi_2\cdots\chi_a\chi_b\cdots\chi_N\rangle. \tag{2.26}$$

When placing N electrons in $2K$ spin orbitals, it yields $\binom{2K}{N}$ different possible determinants (configurations), in which the HF ground state determinant is the lowest in energy. All the other determinants are approximate representations of excited states, which can be generated by promoting one or more electrons from the occupied spin orbitals to the virtual ones.

Given a complete set of spin orbitals $\{\chi_i\}$, a complete and orthonormal set of N-electron determinants can be formed, $\{|\Psi_i\rangle = |\Psi_0\rangle, |\Psi_a^r\rangle, |\Psi_{ab}^{rs}\rangle, |\Psi_{abc}^{rst}\rangle, ...\}$, which can be used as a basis set to expand an arbitrary N-electron wavefunction. The exact many-electron wavefunction can be expressed as a linear combination of all possible N-electron Slater determinants. Using $|\Psi_0\rangle$ as the reference state, the exact electronic wavefunction for any state of the system can be written as:

$$|\Psi\rangle = c_0|\Psi_0\rangle + \sum_{a,r} c_a^r|\Psi_a^r\rangle + \sum_{\substack{a<b\\r<s}} c_{ab}^{rs}|\Psi_{ab}^{rs}\rangle + \sum_{\substack{a<b<c\\r<s<t}} c_{abc}^{rst}|\Psi_{abc}^{rst}\rangle + \cdots, \tag{2.27}$$

where all unique pairs of occupied and unoccupied spin orbitals are included in the expansion. The determinant $|\Psi_a^r\rangle$ represents a singly excited state, where an electron in the occupied spin orbital χ_a has been promoted to the virtual spin orbital χ_r. Similarly, the determinants $|\Psi_{ab}^{rs}\rangle$ and $|\Psi_{abc}^{rst}\rangle$ correspond to doubly excited and triply excited state. The coefficients c_i are determined variationally. The approach in solving Eq. 2.27 is the configuration interaction. Within the BO-approximation, CI provides an exact ground state wavefunction associated with the exact non-relativistic ground state energy of the system, $\mathscr{E}_0$. The difference of this exact energy and the Hartree-Fock energy (E_0) is the correlation energy in the limit of complete basis set:

$$E_{coor} = \mathscr{E}_0 – E_0. \tag{2.28}$$

Clearly, the CI approach for finding the complete solution to the many-electron problem cannot be implemented in practice. It is computationally impossible to handle an infinite basis set of N-electron determinants, which in turn are formed from an infinite set of spin orbitals. Nevertheless, exact solutions to the SE can be found when a finite set of spin orbitals is used, χ_k, providing the set of $\binom{2K}{N}$ determinants. This method is known as *full* CI. For a finite basis set, full CI is the best calculation one can do. The difference between the ground state energy obtained from a HF calculation and a full CI, respectively, using the same basis is called the the basis set correlation energy. As the basis set enlarges, the basis set correlation energy will approach the exact correlation energy.

Full CI is only feasible for small systems, as the number of configurations rapidly increases with the system size. For this reason, it is common practice to truncate the Eq. 2.27 at some excitation level. For instance, one can considered both single and double excitations, giving a singly and doubly excited CI (CISD). A major drawback of almost all forms of truncated CI is that they are not size consistent. This means that the energy of two non-interacting molecules is not twice the energy of one of them. As such, truncated CI describes the electronic energy well around the equilibrium, but the quality quickly decays with the dissociation. Adding

higher excitations (quadruple) can make CI size-consistent for small molecules, though with extra computational expense. The substantial computational cost and the lack of size-consistency of truncated CI have encouraged the development of other post-HF methods such as coupled cluster and many-body perturbation theory. The coupled cluster has emerged as perhaps the most reliable, yet computationally affordable method for approximating the electronic structure. Both of these methods are throughout derived in the textbook of Szabo and Ostlund [7].

2.4 Density Functional Theory

Density functional theory (DFT) offers an alternative approach to describe the electronic structure of a system. The basic idea is that the electronic energy can be expressed as an energy functional of the electron density, denoted $E[\rho(\boldsymbol{r})]$. An important advantage of using the electron density rather than the wavefunction is the significant reduction in dimensions. The density is always three dimensional irrespective of the number of electrons, while the wavefunction involves $3N$ coordinates. For this reason, DFT can be applied for larger systems and has become very popular approach.

The field of DFT is based on two fundamental theorems formulated by Hohenberg and Kohn and the derivation of a set of equations by Kohn and Sham. The theorems establish the relationship between the total electronic energy and the electron density. The first theorem states that the ground state properties are uniquely defined by the electron density. This allows the energy functional of the ground-state density to be written as:

$$E[\rho(\boldsymbol{r})] = T[\rho(\boldsymbol{r})] + V_{eN}[\rho(\boldsymbol{r})] + V_{ee}[\rho(\boldsymbol{r})], \tag{2.29}$$

where the terms represent the kinetic energy of the electrons, the coulomb interaction between the electron density with the fixed nuclei, and the electron-electron interactions, respectively. The second theorem states that the density that minimizes the total energy is the true ground-state density, i.e the density is variational. When the energy is minimizing with respect to the electron density, it imposes a constraint on the density to ensure a conservation of the total number of electrons:

$$\frac{\delta}{\delta\rho(\boldsymbol{r})}\left(E[\rho(\boldsymbol{r})] - \mu\int\rho(\boldsymbol{r})d\boldsymbol{r}\right) = 0, \tag{2.30}$$

where δ denotes a functional derivative, and μ is a Lagrangian multiplier for the constraint. The ground-state electron density must satisfy:

$$\frac{\delta E[\rho(\boldsymbol{r})]}{\delta\rho(\boldsymbol{r})} = \mu, \tag{2.31}$$

which is the fundamental of DFT. Eq. 2.31 may also be regarded as the DFT equivalent to the Schrödinger equation.

Although the Hohenberg and Kohn theorems confirm the uniqueness and existence of the energy functional, its explicit form is unknown. In order to derive a set of solvable equation, Kohn and Sham considered a reference system consisting of N_e non-interacting electrons in an external potential, such that the electron density of the reference system, $\rho_{ref}(\boldsymbol{r})$, is identical to the true density $\rho(\boldsymbol{r})$. The total energy functional can be written in terms of the reference system functional with a additional correction term:

$$E[\rho(\boldsymbol{r})] = T_{ref}[\rho(\boldsymbol{r})] + V_{eN}[\rho(\boldsymbol{r})] + J[\rho(\boldsymbol{r})] + E_{XC}[\rho(\boldsymbol{r})], \tag{2.32}$$

where the corrected exchange-correlation energy is defined as:

$$E_{XC}[\rho(\boldsymbol{r})] = (T[\rho(\boldsymbol{r})] - T_{ref}[\rho(\boldsymbol{r})]) + (V_{ee}[\rho(\boldsymbol{r})] - J[\rho(\boldsymbol{r})])\,. \tag{2.33}$$

The electron repulsion functional, $V_{ee}[\rho(\boldsymbol{r})]$, is a sum of two terms; a classical coulomb contribution, $J[\rho(\boldsymbol{r})]$, and an exchange contribution ($V_{ee}[\rho(\boldsymbol{r})]-J[\rho(\boldsymbol{r})]$). The exchange-correlation term contains the kinetic energy error associated with the reference system, the electronic correlation of the electrons, and the electronic exchange. The density can be represented as a set of one-electron orthonormal orbitals:

$$\rho(\boldsymbol{r}) = \sum_{i}^{N} |\varphi_i(\boldsymbol{r})|^2. \tag{2.34}$$

Then, the kinetic energy of non-interacting electrons with the true density can be written as:

$$T_{ref}[\rho(\boldsymbol{r})] = -\frac{1}{2}\sum_{i} \langle\varphi_i|\nabla^2|\varphi_i\rangle d\boldsymbol{r} d\boldsymbol{r}', \tag{2.35}$$

and the electrostatic energy between two charge densities within the Hartree approach:

$$J_H[\rho(\boldsymbol{r})] = \frac{1}{2}\int\int \frac{\rho(\boldsymbol{r})\rho(\boldsymbol{r}')}{|\boldsymbol{r}-\boldsymbol{r}'|} d\boldsymbol{r} d\boldsymbol{r}'. \tag{2.36}$$

The XC functional is defined as the functional derivative of the XC energy term:

$$V_{XC}(\boldsymbol{r}) = \frac{\delta E_{XC}[\rho(\boldsymbol{r})]}{\delta\rho(\boldsymbol{r})}. \tag{2.37}$$

Expressing the remaining energy terms as above, it results in a set of eigenvalue equations that can be solved in a self-consistent approach:

$$(V_{eN} + V_{KE} + V_H + V_{XC})\varphi_i(\boldsymbol{r}) = \epsilon_i\varphi_i(\boldsymbol{r}). \tag{2.38}$$

where ϵ_i are the orbital energies. This is known as the Kohn-Sham equations. If the exchange-correlation term can be exactly determined, DFT would yield the exact ground state electronic energy. Unfortunately, its exact form turns out to be quite difficult to find. Several approaches have been developed to approximate this term. Two of them are described briefly in the following sections according to Leach [10].

2.4.1 Local density approximation

The original paper of Kohn and Sham has also introduced a simple method to approximate the exchange-correlation functional, known as local density approximation (LDA). Based on the uniform electron gas (UEG) model, the electron density is assumed to be slowly varying, and thus, treated locally. Using this, LDA assumes that at each point $\boldsymbol{r}$, where the density is $\rho(\boldsymbol{r})$, the exchange-correlation energy is the same as that of a uniform gas of the same density:

$$E_{XC}^{LDA}[\rho(\boldsymbol{r})] = \int \rho(\boldsymbol{r})\varepsilon_{XC}(\rho(\boldsymbol{r}))d\boldsymbol{r}, \tag{2.39}$$

where ε_{XC} is the exchange-correlation energy per electron of a uniform gas of density $\rho(\boldsymbol{r})$. For the uniform electron gas, ε_{XC} for all densities can be accurately computed by Monte Carlo. Moreover, the term ε_{XC} can be split into exchange and correlation contributions:

$$\varepsilon_{XC}(\rho(\boldsymbol{r})) = \varepsilon_X(\rho(\boldsymbol{r})) + \varepsilon_C(\rho(\boldsymbol{r})), \tag{2.40}$$

where each term is considered separately. Approximation errors of exchange and correlation terms tend to cancel each other, as the underestimation of exchange energy compensates for the overestimation of correlation.

LDA forms the basis of all approximate exchange-correlation functionals. Despite its simplicity, LDA provides remarkably accurate results for certain applications, and improvements are constantly developing to cover the shortcomings of LDA in describing properties such as binding energy, hydrogen bonding and weak interactions. For some applications, including only the density is somewhat deficient, such that its gradient must also be included.

2.4.2 Generalized gradient approximation

In situations where the density varies considerably, LDA might fail as it is based on the uniform electron gas model. To improve the LDA method, the gradient of the density at each point in space is additionally incorporated to the functional. The approach is called generalized gradient approximation (GGA). The exchange-correlation functional takes the general form

$$E_{XC}^{GGA}[\rho(\boldsymbol{r})] = \int d^3r f(\rho(\boldsymbol{r}), \nabla\rho(\boldsymbol{r})). \tag{2.41}$$

Since there are many ways to include the information from the gradient in a GGA, there exists a large number of distinct GGA functionals. Two of the most widely used functionals are the Perdew-Wang functional (PW91) and the Perdew-Burke-Ernzerhof functional (PBE). Although it is tempting to assume that GGA must be more accurate than LDA, as more information is included. Unfortunately this is not always the case. In the optimization process of the force field, discussed in the next chapter, DFT is applied with PBE functionals in the Amsterdam Density Functional software (ADF) to calculate training data.

Chapter 3

Empirical reactive force field

This chapter introduces the reactive force field, $\text{ReaxFF}_{\text{NaC}}$, that has been constructed to study sodium diffusion in graphite. The general features of force fields are briefly described in first, and the majority of this part is drawn from *Molecular modelling* by Leach [10]. The mathematical formalism of reactive force field and the parametrization process are outlined in details, followed with the optimization and simulation results. The resulting force field is further applied as in this thesis to study sodium diffusion in amorphous carbon at room temperature.

3.1 Empirical force field

For many molecular systems of interest, the number of atoms are too large to be considered with quantum mechanics due to the computational resources required. One must then resort to molecular mechanics (MM) methods, also known as empirical force fields (FF). These methods do not consider the electrons explicitly, and calculate the potential energy as a function of the nuclear position. Hence, force fields allows systems containing significant number of atoms to be studied, where the calculations can be performed in a fraction of the computer time. Although force field approaches are much more approximate compared to *ab initio* and often considered to be less accurate, sophisticated force fields developed today provide a comparable high level of accuracy.

The force field or the potential function consists of an empirical set of energy functions describing bonded and non-bonded interaction. Each energy function contains several atom-type parameters, i.e the same parameter has a different value for each type of atom, to be determined. For a basic force field, the bonded terms include bond stretching, angle bending and torsional rotation, and non-bonded comprise of van der Waals interaction and electrostatic interaction. Other energy terms such as hydrogen bonding can be included. Since force fields are empirical, there is not an “exact”or“more correct ”form of the potential function. Each energy term can thus take different functional forms. Most available force fields do have very similar function form. For instance, the van der Waals term is often modeled with a Lennard-Jones potential, and the electrostatic interaction with a Coulomb potential.

All force fields aim to be as general as possible and allow predictions for several classes of compound.

This is referred as the transferability of the force field, which essentially means that same optimized set of parameters used to model a particular molecule, could be applied to model other related molecules, instead of defining a new set. The transferability is very important when making new predictions, and it is not easy to achieve. The set of parameters is typically determined from fitting to different experimental or higher-level computational data. Some are even parametrized to predict certain properties. Hence, the individual parameters are in general not transferable between different force fields. Due to specific parametrization, some force fields may be better suited for studying specific problems or classes of molecules.

Traditional force fields often rely on a predefined set of bonds. During simulations, the bonds are kept constant and not permitted to form or break, leading to a fixed connectivity of the molecular system. Consequently, these force fields are unable to describe the chemical reactivity of a system during simulations, forfeiting the important dynamical properties of atoms. Several force fields have been developed to incorporate the breaking and forming phenomena of bonds during dynamics. The arguably most successful is the reactive force field (ReaxFF) introduced by van Duin *et al.*, which is outlined in the next section.

3.2 Reactive force field

Reactive force field was initially developed by van Duin and coworkers [11] to study hydrocarbons. Since then it has been successfully applied to model a wide range of compounds [12]. ReaxFF uses the bond-order concept to model interactions, enabling the description of chemical reactions such as bond breaking and forming during simulation. Moreover, ReaxFF calculates non-bonded interactions such as Coulomb and van der Waals forces between all atoms, regardless connectivity, making it suitable for systems with both covalent and ionic interactions. In addition, ReaxFF display modest scaling with the system size, and can be trained against small relevant systems *ab initio* calculations on a training set of reactions.

3.2.1 ReaxFF scheme

The force field for reactive systems divides the total energy into partial energy contributions as follow:

$$E_{system} = E_{bond} + E_{over} + E_{under} + E_{val} + E_{tors} + E_{vdWaals} + E_{Coulomb}, \tag{3.1}$$

where it includes bond, over-coordination penalty, lone-pair, valence, torsion, non-bonded interactions, such as van der Waals and Coulomb energies, respectively. The detailed explanation of each energy term can be found in various publications [11–13]. Fig. 3.1 illustrates systematically the calculation steps during simulation, where the bonded and non-bonded terms are calculated separately [13].

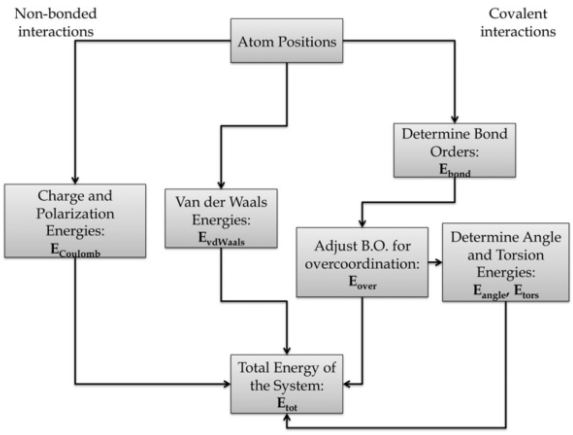

Figure 3.1: ReaxFF iteration scheme during the simulation [13].

For the sodium-carbon system of interest, the energy equation reduces to these four terms:

$$E_{system} = E_{bond} + E_{over} + E_{under} + E_{vdWaals} + E_{Coulomb}. \tag{3.2}$$

The first term E_{bond} describes the energy associated with bonding between atoms, E_{over} is an energy penalty adjusting the over coordination of atoms and E_{under} ensures correct bond order for under-coordinated system. The non-bonded $E_{Coulomb}$ and $E_{vdWaals}$ are the electrostatic and dispersive energy contributions that are calculated for all atoms. Since the bonds sodium-carbon and sodium-hydrogen are largely ionic, the angle bending and torsional term are set equal to zero and do not contribute to the total energy. All equations associated with the relevant energy terms in Eq. 3.2 can be found in Appendix A. These terms are further described in fairly details as reported by Ref. [11, 14].

As seen in Fig. 3.1 the first step is to determine the dynamic bond order of all atom pair in the system. ReaxFF calculates the total *uncorrected* bond order between a pair of atoms i and j as a sum of the sigma, pi, and double pi bond order contributions:

$$\begin{aligned} BO'_{ij} &= BO'^{\sigma}_{ij} + BO'^{\pi}_{ij} + BO'^{\pi\pi}_{ij} \\ &= exp\left[p_{bo,1} \cdot \left(\frac{r_{ij}}{r_0^{\sigma}}\right)^{p_{bo,2}}\right] + exp\left[p_{bo,3} \cdot \left(\frac{r_{ij}}{r_0^{\pi}}\right)^{p_{bo,4}}\right] + exp\left[p_{bo,5} \cdot \left(\frac{r_{ij}}{r_0^{\pi\pi}}\right)^{p_{bo,6}}\right], \end{aligned} \tag{3.3}$$

where r_{ij} is the interatomic distance between atoms i and j , and r_0^{μ} is the equilibrium distance for the given bond between these atoms. The bonding term p_{bo} and bonding equilibrium distance r_0 are parameters to be determined. Since the bonding interactions are regarded at a large distance, ReaxFF can accurately model the long range, partially bonded configurations of transition states. When including long range interactions, the bond orders can be overestimated due to weak attraction of the nearest neighbors, and lead to inaccurate behavior when modeling bonded molecules. Depending on the surrounding geometry, each of the three partial bond orders in Eq. 3.3 is corrected to give the *corrected* bond orders, BO^{μ}_{ij}. When an atom has more bonds than its valence allows, the long range interactions with its neighbors is reduced to minimize their effects. Conversely, when the atom has less than its optimal bond order, these weak interactions are allowed. The

final bond orders are corrected twice. The bond energy E_{bond} is a function of the corrected bond order, the respective dissociation energies of each component of the bond and two additional parameters p_{be1} and p_{be2}:

$$E_{bond} = -D_e^{\sigma} \cdot BO_{ij}^{\sigma} \cdot exp\left[p_{be1}(1 - (BO_{ij}^{\sigma}))^{p_{be2}}\right] - D_e^{\pi} \cdot BO_{ij}^{\pi} - D_e^{\pi\pi} \cdot BO_{ij}^{\pi\pi}. \tag{3.4}$$

Although the bond orders are corrected, some degree of overcoordination may remain in the molecule. To overcome this, an overcoordination penalty term has to be added to the force field. For an overcoordinated atom, an energy penalty E_{over} is imposed on the system, and E_{over} goes quickly to zero for undercoordinated system. For an undercoordinated atom, the energy contribution of pi electron between undercoordinated atomic centers E_{under} is taken to account.

At short interatomic distances there are repulsive interactions due to the Pauli principle, and at long distances attraction energies arise due to dispersion. These non-bonded interactions are the Coulomb and van der Waals forces, respectively. Unlike the non-reactive force field where these forces are calculated only between atoms that do not share a bond, ReaxFF calculates these forces for all atoms, regardless of their connectivity. To prevent high interaction between atoms sharing bond and bond angle at close distances, a shielding term γ_{ij} is included for both interaction forces. The Coulombic interaction is calculated by:

$$E_{Coulomb} = Tap \cdot C \cdot \frac{q_i \cdot q_j}{\left[r_{ij}^3 + \left(\frac{1}{\gamma_{ij}}\right)^3\right]^{\frac{1}{3}}}. \tag{3.5}$$

To ensure a smooth cut-off, $E_{Coulomb}$ is scaled by a seventh order Taper-polynomial T [15, 16]. The atomic charges q_i and q_j can be assigned in numerous ways. Two common methods often coupled in force fields are the Electron Equilibrium Method (EEM) approach by Mortier *el al.* [17] and the *charge equilibration method* (QEq) by Rappé and Goddard [18], which is based on the former. These method are able to rapidly feed the dynamic charges into Eq. 3.5 during simulation. The atomic charges are connectivity and geometry dependent. Both methods are based on the electronegativity equalization principle of Sanderson [19], stating that the electronegativities of the atoms forming the molecule are equal to the molecular electronegativity.

The van der Waals energy contribution is given as:

$$E_{vdW} = Tap \cdot E_{ij}^{vdW} \cdot \left\{ exp\left[\alpha \cdot \left(1 - \frac{f_{13}(r_{ij})}{r_{vdW}}\right)\right] - 2 \cdot exp\left\{\frac{1}{2} \cdot \alpha_{ij} \cdot \left(1 - \frac{f_{13}(r_{ij})}{r_{ij}^{vdW}}\right)\right]\right\}, \tag{3.6}$$

$$f_{13}(r_{ij}) = \left[r_{ij}^{p_{vdW1}} + \left(\frac{1}{\gamma_{ij}^{vdW}}\right)^{\frac{1}{p_{vdW1}}}\right]^{\frac{1}{p_{vdW1}}}. \tag{3.7}$$

The distance-corrected shielding term γ_{ij}^{vdW} is included to prevent repulsive interactions between bonded atoms. The term E_{ij}^{vdW} is the dissociation energy of the Morse-potential, r_{ij}^{vdW} is the van der Waals radius of the atom pair and α_{ij} controls the shape of the potential. These parameters are empirical. In addition, a recently developed "inner-wall "van der Waals shielding term described by [20] is also included in the training set. The term is not included in the original framework of ReaxFF. Although it is developed for high velocity impact, it might be significant for the Na-C system.

3.2.2 Force field parameterization

The optimized force field for sodium-carbon system ($\text{ReaxFF}_{\text{NaC}}$) has been parametrized by Hjertenæs [4]. The optimization process and results summarized here, together with MD simulation results can be found this publication.

The objective of the parameter set for NaC was to study sodium diffusion and interaction in graphitic carbon cathode in aluminum electrolysis. The parameter set consisted of 95 parameters, involving 39 generals, 32 elements and 24 pair parameters. Determining all 95 parameters from scratch would be an extensive process. It was decided to adopt parameters from similar studies in order to reduce the number of them. The general parameters for carbon and hydrogen, both atomic and pair-parameters, were adopted from a lithium-carbon parameter set optimized by Raju and co-workers [21]. The particular lithium-carbon parameter set also served as the starting point for the parameterization process. The atomic sodium parameters, and the sodium-hydrogen off-diagonal and pair parameters were chosen from the sodium-hydride force field developed by Ojwang [22]. The remaining parameters to be optimized were the sodium-carbon pair and off-diagonal parameters. Adopting parameters from other studies was a somewhat risky choice, as the performance of the optimized force field depended greatly on the quality of these. However, by doing so, the respective behaviors of sodium and lithium could be carefully compared.

Fig. 3.2 and 3.3 display the small training systems representative of the sodium-graphite system being studied. The training data involved geometries, formation energies, potential energy surfaces (PES) and atomic charges from these complexes. The phenylsodium in Fig. 3.2a represented the covalent bond between sodium and aromatic carbon, Fig. 3.2b illustrated a single sodium atom adsorbed on polycyclic aromatic hydrocarbon (PAH) and Fig. 3.2c-e various sodium clusterings. Two types of defective graphene were considered; a single vacancy defect (SD) and a double vacancy defect (DD). Fig 3.3 shows sodium clusters adsorbed on pristine and defective graphite, with and without SD and DD, in which hydrogen atoms were excluded for clarity. Moreover, the jump barrier of sodium atom intercalated between PAHs, Fig. 3.6, were included in the training set. All training data were computed using DFT with the generalized gradient

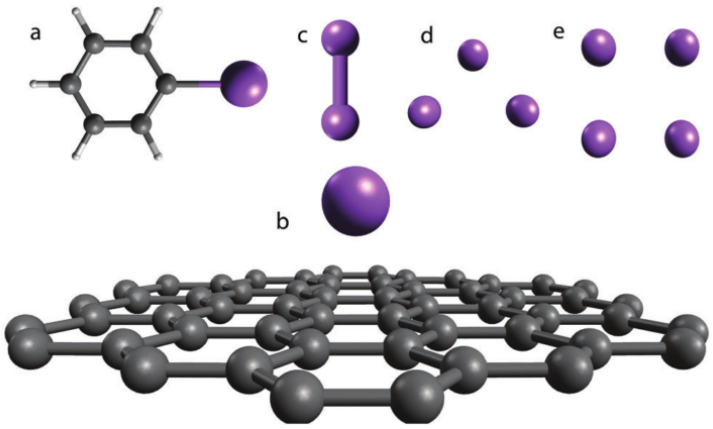

Figure 3.2: Relevant systems used to train the force field parameters. a) Phenylsodium: equilibrium geometry and full potential energy curve of the dissociation of the C–Na bond, b) sodium adsorbed on a circumcoronene ($C_{54}H8$): equilibrium geometry and full adsorption curve, c–e) sodium clusters: bond energies and equilibrium geometry. Full potential energy curve for the dissociation of Na_2.

approximation (GGA) by Perdew, Burke and Ernzerhofer (PBE) [23] together with the QZ4P basis set [24] in ADF [25]. The parameters to optimize were the sodium–carbon pair and off-diagonal parameters, as well as the introduced inner-wall van der Waals correction added to the sodium atomic parameters [20]. The optimization process was carried out using the Metropolis Monte Carlo (MC) routine developed by Iype *et al.* [26]. The routine effectively minimized an error-function by randomly making changes to the "open 'parameters in the force field:

$$Error = \sum_i \left[\frac{\left(x_i^{trained} - x_i^{ReaxFF}\right)^2}{\sigma_i} \right], \tag{3.8}$$

where the parameter σ_i was an inverse weight and was adjusted to balance the error function. The inverse weights included the weight of bond length (0.1Å), of bond angle (2 degrees) and of energy difference (0.1-1.0 kcal mol^{-1}). Following the simulated annealing process described by Iype, several heating cycles were performed for each error function. The error function itself did not carry any physical meaning. The changes made by each MC move as well as the associated weights, were fine-tuned in order to obtain a good balance between the training systems.

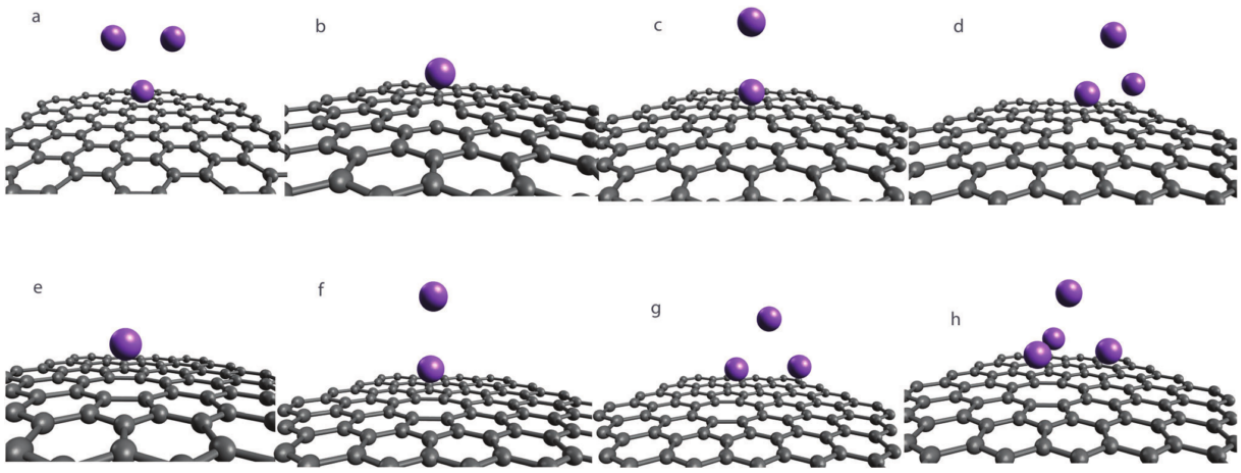

Figure 3.3: Sodium clusters on circumcircumcoronene ($C_{96}H_{24}$), with and without defects, either single vacancy defect or double vacancy defect. Na and Na_2 on pristine graphite have been excluded from the figure.

Atomic charges used in the calculation of electrostatic contribution were computed with the electronegativity equalization method (EEM) [27]. The atomic charges were obtained by solving a coupled set of equations based on the two parameters; electronegativity, χ_{Na}^{EEM}, and the chemical hardness, η_{Na}^{EEM}. These EEM-parameters for sodium were separately trained against the multipole derived charges, up to quadrupole moments (MDC-q). The method described by Swart and co-workers [28] calculated atomic charges from the atomic multipole moments. The atomic charges were considered for a sodium atom adsorbed on a circumcoronene molecule ($C_{54}H_{18}$) and sodium intercalated between two eclipsed coronene molecules ($C_{24}H_{12}$) in the central hexagonal site and at the saddle point between two hexagonal sites.

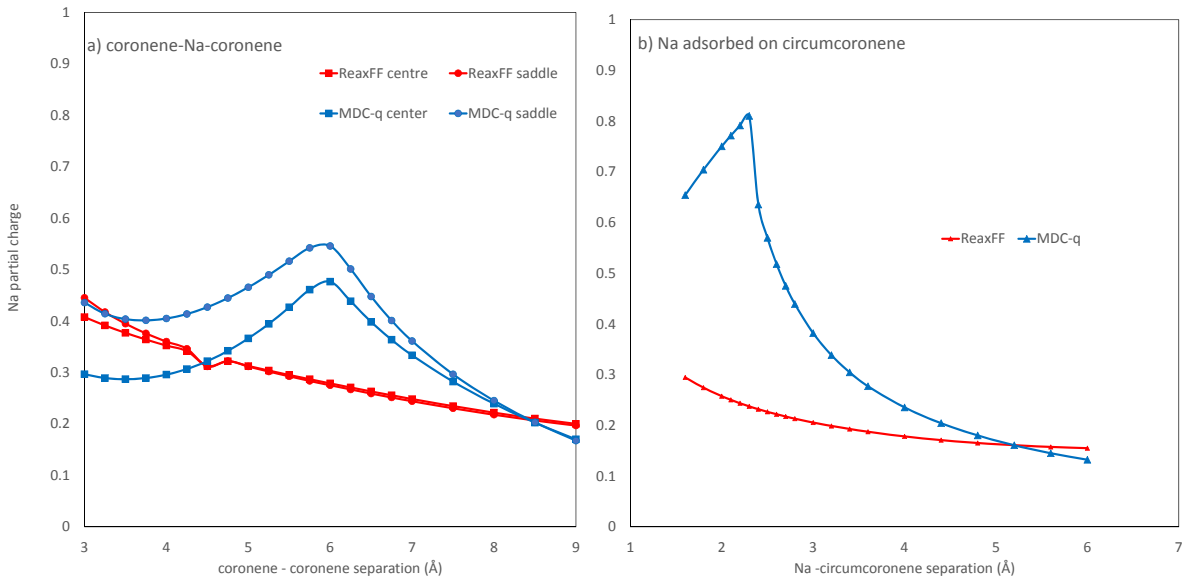

Figure 3.4: Atomic charges calculated with DFT/PBE and the force field optimized for sodium intercalated between two eclipsed coronene molecules separating from 3 to 5.5 Å, and for sodium adsorbed on circumcoronene.

3.2.3 Force field optimization

Fig. 3.4 shows the partial charges of intercalated and adsorbed sodium, respectively, and compares the predicted atomic charges from the optimized set of EEM-parameter with the training data computed with MDC-q. Clearly, there were several limitations of the EEM method. The method was unable to predict the correct charge of a sodium intercalated between two coronene. Atomic charges predicted by MDC-q exhibited a distinct peak at a PAH-PAH separation of about 6Å at both center and saddle site. This qualitative behavior of atomic charge was not detected by EEM. In addition, EEM did not capture the steep increase in atomic charge of a sodium atom adsorbed on a PAH. Due to the limitations with the EEM framework the calculated charges from the optimized force field were only for qualitative use.

The parameters electronegativity χ_{Na}^{EEM} and chemical hardness η_{Na}^{EEM} were kept fixed while the remaining open parameters were trained against potential energy curves and equilibrium geometries. When considering the bonding between sodium and carbon, there were two main aspects: 1) the covalent bond between sodium and aromatic carbon, i.e. phenylsodium shown in Fig. 3.2a, and 2) the adsorption of sodium onto PAHs shown as a circumcoronene in Fig. 3.2b. In the ReaxFF formalism, these bonding types were obtained from energy contributions of covalent bond energy, van der Waals and electrostatic terms. The bonded term, including all three types bonding interactions, was computed from an energy function of bond order, which in turn was a dynamic function of the interatomic distances. The shape of the dissociation profile was controlled by several bond-order parameters and the dissociation energy, depending on the molecular environment through bond-order correction parameters. Both non-bonded interactions were calculated between all atom pairs and scaled with a taper polynomial to ensure a smooth cut-off. The Coulomb electrostatic energy term used the optimized EEM-charges and a third-order shielding in the atomic separation.

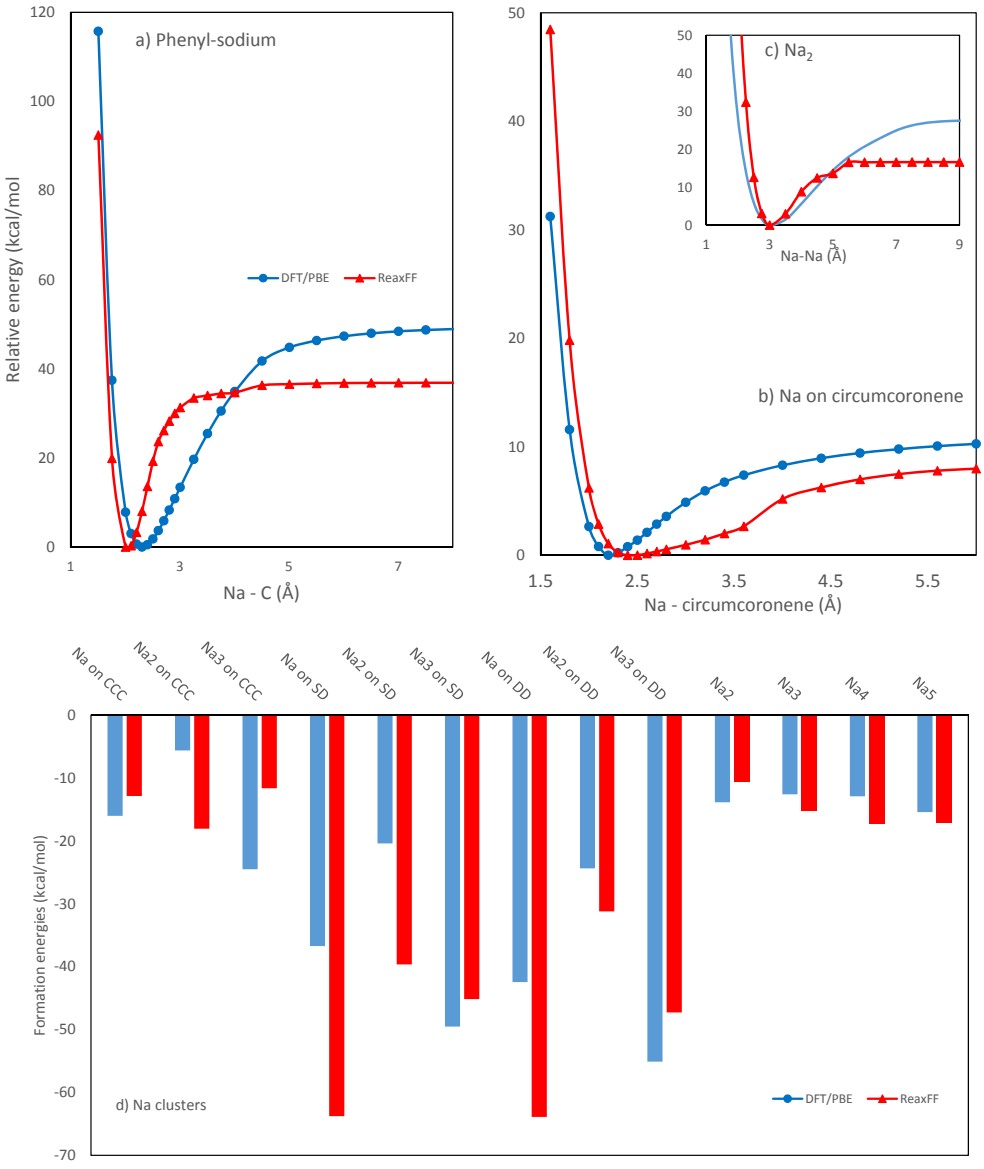

Figure 3.5: Dissociation energies and bond energies as training data calculated by DFT/PBE and by ReaxFF.

Fig. 3.5 and 3.6 show the reproduction of the training data obtained with the optimized force field. The top of Fig. 3.5 shows the dissociation energies of phenylsodium, adsorbed sodium on a PAH and sodium dimer Na_2. The dissociation curves obtained by ReaxFF overall exhibited quite similar behavior to those of DFT. In addition, ReaxFF estimated comparable equilibrium bond lengths to those of DFT. The lower part of Fig. 3.5 shows bond energies calculated by DFT and by ReaxFF. The average deviation in the formation energy of sodium atoms and clusters on pristine and defective PAHs was 13 kcal mol^{-1}, which was quite significant. As seen from the figure, the largest deviation was the adsorption energy of sodium dimer on PAH. The overestimation of energy of Na_2-PAH was probably due to the inadequate overcoordination penalties and bond-order corrections. Alleviating this effect was not possible in the parameter set without compensating for some loss in accuracy for other complexes. Finally, the force field was used to recalculate the jump barrier between hexagonal sites of a sodium atom intercalated between two coronenes. Fig. 3.6 shows a good agreement of these energy barriers, with a minor deviation of the one obtained from ReaxFF. In summary, the resulting parameter set reproduced the training data with moderate accuracy and acceptable precision.

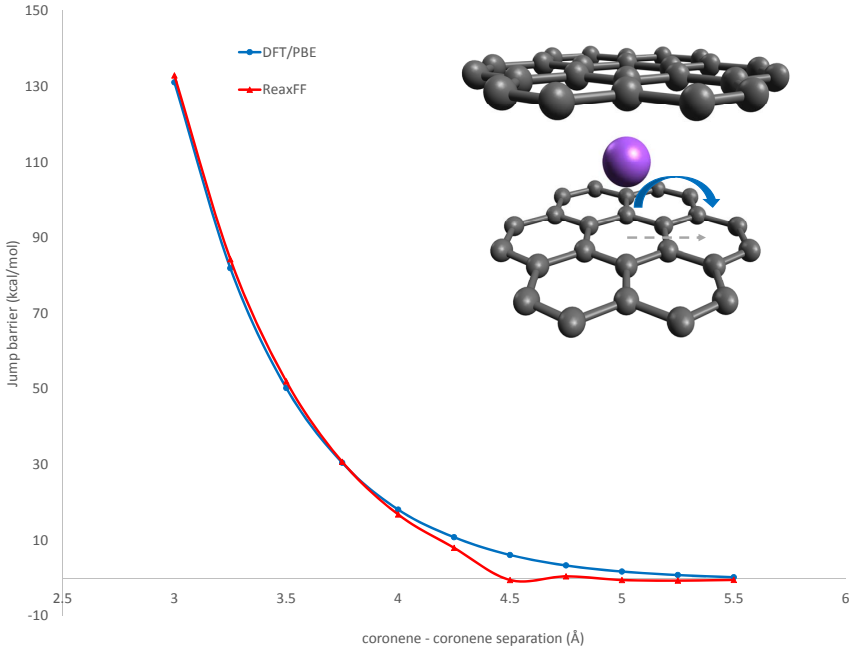

Figure 3.6: Jump barrier between hexagonal sites in a coronene-Na-coronene complex with respect to the separation of coronenes.

3.2.4 Force field predictions

One essential feature of a force field is the ability to predict relevant data that has not been included in the training set. In this section, the predicted results are presented and compared accordingly with data derived from DFT to demonstrate the predictive power of the force field.

The first distinctive feature was a correct balance between the sodium-sodium covalent bond and the adsorption of sodium on PAHs. Fig. 3.7 shows the bond energies of two sodium atoms adsorbed on a circumcoronene

associated with the respective spacings between the sodium atoms and the carbon layer and adsorption sites. Overall, the ReaxFF predicted bound energies that agreed quite well with DFT-results. The average absolute deviation was of 5 kcal mol^{-1}. As seen in Fig. 3.7, the bond energy of the rightmost structure had the lowest energy calculated by both DFT/PBE and ReaxFF, suggesting that this was the equilibrium geometry. However, sodium atoms adsorbed 3.2 Å with a separation of 3.2 Å between them was an actually offset from the "normal "hexagonal adsorption sites.

After studying the adsorption characteristic of sodium atoms on carbon graphite layer, the next obvious feature of interest was the possible diffusion paths. Graphite has two characteristic planes: a basal plane and an edged plane, each exhibiting different physical and chemical activity in many aspects. Diffusion of sodium through the basal plane is prohibited by the high energy barrier and can only be facilitated by defects such as vacancies. Fig. 3.8 shows the potential energy curves of a single sodium atom passing through pristine circumcircumcoronene and those with single and double defect. As observed, the barrier heights calculated by ReaxFF deviated considerably from those obtained by DFT/PBE-QZ4P, especially for the cases with defects. However, the relative order and magnitudes of the respective barriers displayed moderate accuracy.

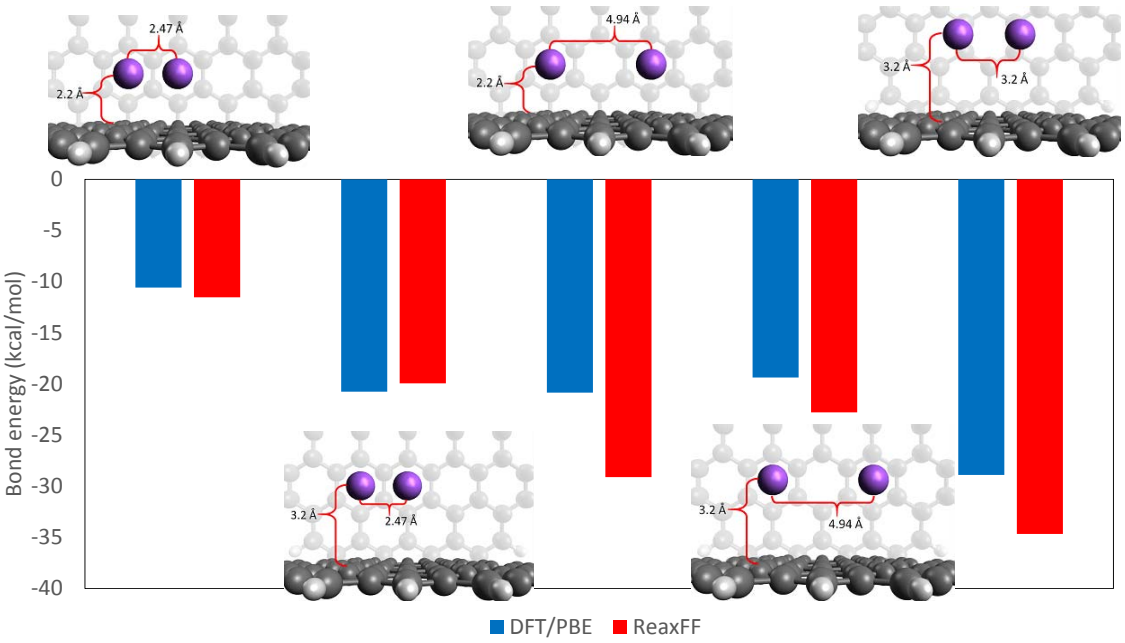

Figure 3.7: Bond energies of two sodium atoms adsorbed on a circumcoronene molecule, calculated with DFT and predicted by the optimized $ReaxFF_{NaC}$.

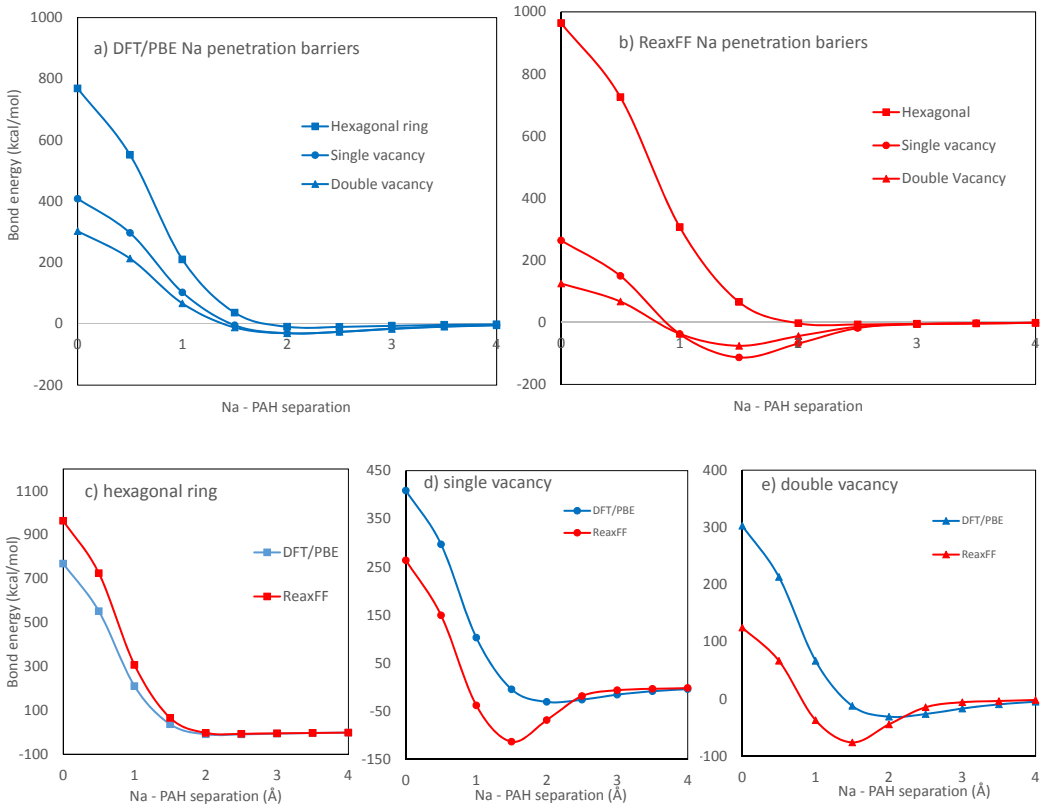

Figure 3.8: Diffusion barrier of sodium atoms through a hexagonal site, a single vacancy, and a double vacancy in a circumcircumcoronene. The top two figures display the diffusion profiles for the three pathways computed with DFF and ReaxFF, and the bottom three compare each pathway individually.

Another diffusion path is through an edge plane of the graphite crystallite. In the training set, an energy barrier of a jump between hexagonal sites in an eclipsed coronene (AA-stacked graphite) was included. Prior to sodium intercalation, the graphene layers in graphite were stacked in an AB-sequence. They effectively shifted to AA-sequence when sodium intercalated, resulting into the familiar configuration for intercalation compounds. The optimized force field was tested to show its ability to capture the structural change in intercalation compounds. A model system showing in Fig. 3.9 was created consisting of two ABAB-stacked coronene dimers having a interlayer spacing of 3.35 Å and a zig-zag edge plane. The four hydrogen atoms closest to the sodium entry path were removed. A potential energy surface of a sodium atom moving horizontally into the complex was obtained with DFT and ReaxFF, respectively. ReaxFF produced a qualitative good potential energy surface with similar behavior to the one obtained from DFT. ReaxFF overestimated the binding with edge site by 7 kcal mol^{-1}. From this binding edge site, the barrier to enter the complex was determined to 145 kcal mol^{-1} by DFT. ReaxFF overestimated this barrier by 10.8 kcal mol^{-1}.

Many DFT-studies have been performed to estimate the formation energy of alkali metal graphite-intercalation compounds (AM-GIC) [29–31]. The GICs are formed when alkali metals are inserted between the layers upon electrochemical reducing. Most of the studies reasonably agree that the formation energy of sodium intercalation compounds (Na-GIC), unlike those of lithium and sodium, are positive. This essentially means

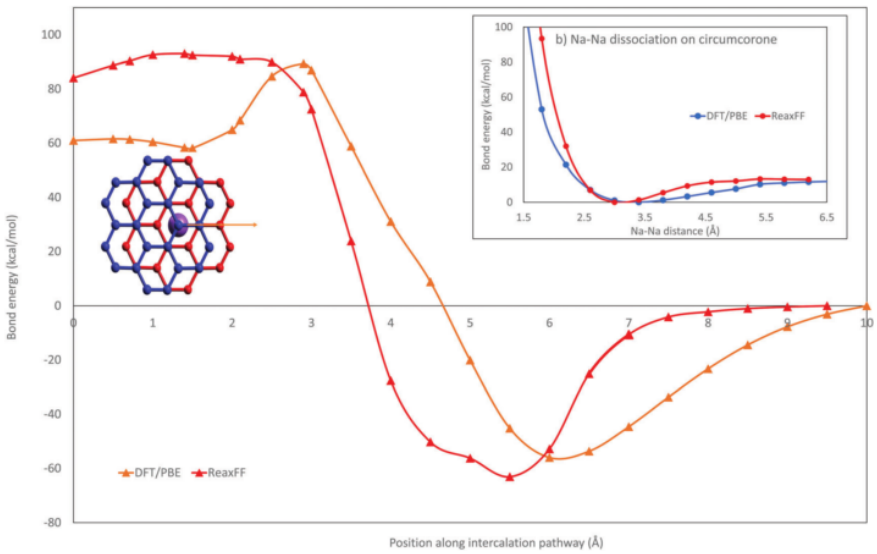

Figure 3.9: Potential energy surface of the sodium atom diffusing the coronene-coronene complex achieved with PBE/QZ4P and ReaxFF.

that Na-GIC are thermodynamically unstable. Applying the developed force field, the body-centered cubic (bbc) structure of sodium metal, the ABAB-stacked graphite and the stage-I Na-GIC (NaC_8) were optimized. Stage-I indicates that graphite layers are completely filled with Na. The sodium parameters produced an optimal bbc sodium metal with a cell parameter of 4.1Å, which was very close to the literature value of 4.23Å. The applied graphitic parameters [21] predicted a graphite structure with the C-C bond of 1.44 Å and interlayer spacing of 3.35 Å, deviating from the literature values 1.421 Å and 3.354 Å, respectively. Fig. 3.10 shows the optimized Na-GIC structure NaC_8, having the interlayer spacing of 3.89 Å, which was lower than the reported DFT-estimated value of ∼4.5 Å. The intra-layer C-C bonds forming the hexagonal sites and accommodating the sodium atoms were shortened to 1.39 Å, while the remaining bonds were elongated to 1.47 Å.

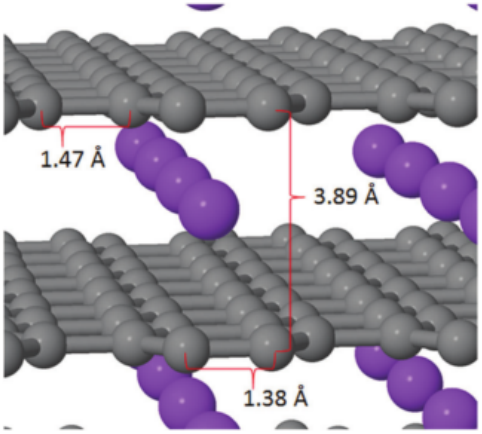

Figure 3.10: Optimized structure of the stage-I sodium graphite intercalation compound using the developed ReaxFF.

Moreover, ReaxFF calculated the formation energy of Na-GIC to be -2.92 kcal mol^{-1}. It severely deviated from the reported DFT values of around $+5$ kcal mol^{-1}. This large inconsistency in energy suggested that the carbon-parameters used in the force field should be re-optimized. The inconsistency was already observed with the optimized graphite structure, and the re-optimized set of carbon-parameters could have yield more accurate GIC structure and hence formation energy. Additionally, the low value of the optimized intra-layer C-C bonds suggested that the covalent C-C bonds were too soft, and that the energy required to reorganize the graphite structure from AB- to AA-stacking was too low, thus leading to a negative energy formation for NaC_8.

3.2.5 Molecular dynamics simulation

Having the optimized force field available, the next step is to perform simulations with molecular dynamics (MD) and hybrid grand-canonical Monte Carlo/MD (GC-MC/MD) [32]. All simulations were carried out in the simulator program LAMMPS [33].

To consider the aspect of sodium diffusion through vacancy defects, a carbon slab was created containing four graphene layers simply stacked in ABAB sequence, each layers having 256 carbon atoms. Two atoms were removed from the top layer to create a double vacancy defect, while the bottom layer had one vacancy defect. Above the slab there was a vacuum void of 18 Å, where the sodium atoms were randomly placed. Increasing densities of sodium vapor were studied. The initial velocities of all atoms were assigned according to the Boltzmann distribution of 300 K. A time step of 0.1 fs was used, and the total simulation time was set to 110 ps. Periodic boundary conditions were applied in all directions. The slab was exposed to sodium vapor in the NVT ensemble. Using the Nose-Hoover thermostat [34], the temperature was carefully increased from 300 to 1200 K. Almost immediately, sodium vapor rapidly adsorbed to the graphite surfaces. In the cases of quite low densities, the surfaces could be covered with all sodium atoms, no free sodium atoms were observed.

Fig. 3.11 shows snapshots taken from the simulation with sodium density of 0.082 g/cm^3, giving a total of 41 sodium atoms per unit cell. After only 2 ps, Fig. 3.11b shows a complete adsorption of sodium atoms on both surfaces. Shown in Fig. 3.11c, after 8 ps, a sodium atom was observed to enter the carbon structure through the double vacancy defect, which was a preferred adsorption site. The entered atom quickly promoted the two top layers to reorganize themselves in an AA-stacking fashion, appearing to interrupt somewhat the weak van Waals forces between the layers. Apart from these weak forces there were nothing preventing the layers to slide relative to each other. Once entered through the double defect, the sodium atom was additionally stabilized by the adsorption to the hexagonal site of the next layer. It resided in this site throughout the remaining simulation, locking the two graphene sheets in the AA-stacking order. No sodium atom entered the single vacancy. The similar sodium entry was qualitatively observed for sodium densities up to 0.732 g/cm^3. At higher densities, the vacuum between the slabs was effectively filled with a sodium vapor, exerting a large pressure on the graphite slab below. This caused the graphene sheets to be pushed together and increased the barrier for further intercalation. As the entry of sodium atom through the double defect happened at an early stage of the simulation, the high barrier restricted the mobility of the single sodium atom in the structure. This showed the moderate strength of sodium intercalation with respect to graphite. A simple structural defect can easily promote sodium intercalation, only one single sodium is sufficient to shift the ideal stacking order and lock it in place.

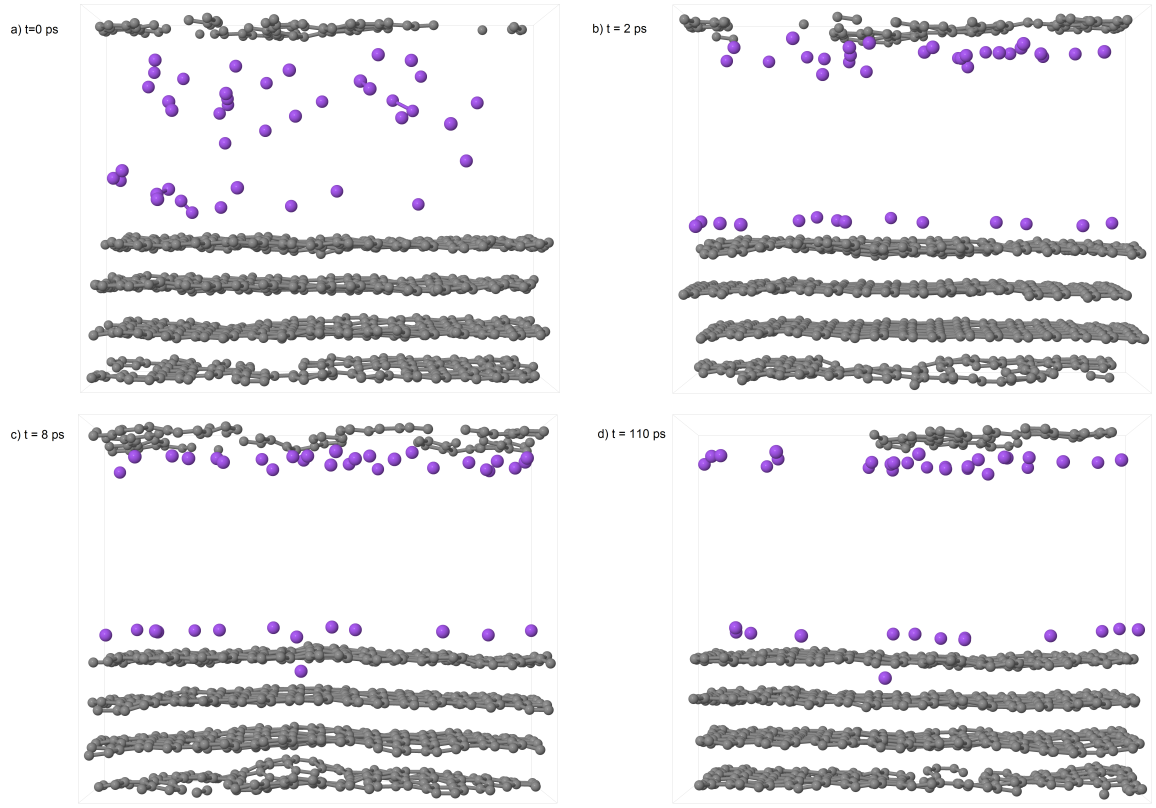

Figure 3.11: Snapshots of graphite slab with single and double defects exposed to sodium vapor of density 0.082 g/cm^3. The first three snapshots were during the temperature increase from 300 to 1200K.

The final structure of interest was a considerably large porous graphite structure as shown in Fig. 3.12. It was constructed to have ten graphene layers stacked in the stable ABAB-configuration, each layer consisting of 384 carbon atoms. A large pore was created in the middle of the unit cell by removing a section of eight middle layers, corresponding to 17 Å along the y-direction and a full length in the x-direction. As such, the porous cell contained open channels along the x-direction, and in the y-direction was a perfect 8 layers crystallite. Keeping the two middle rows fixed along x-direction, the crystallite was locked in position. As followed, the layers were only permitted to move vertically, increasing/decreasing the interlayer spacings, and not shift laterally changing to AA-configuration. Periodic boundary conditions were applied in all directions.

At first, the graphite pore structure was equilibrated at 1200 K and 1 atm. Then, the pore was connected to a reservoir of sodium atoms having the same temperature as the system. Various chemical potentials were applied, as defined by Frenkel and Smith and implemented by Senftle [32]. The simulation was performed with the GC-MC/MD in the NVT ensemble, where for every 1000 MD-step (0.1 fs) ten MC insertions or deletions of sodium atoms were attempted in the cell. It was observed that sodium atoms rapidly bounded to the graphene edges before effectively adsorbed into the open channels. It appeared that the intercalation of sodium occurred spontaneously, and there was no substantial accumulation of sodium in the pore. Keeping the chemical potential higher than a certain threshold would let the insertions continue until the graphite structure was saturated with sodium.

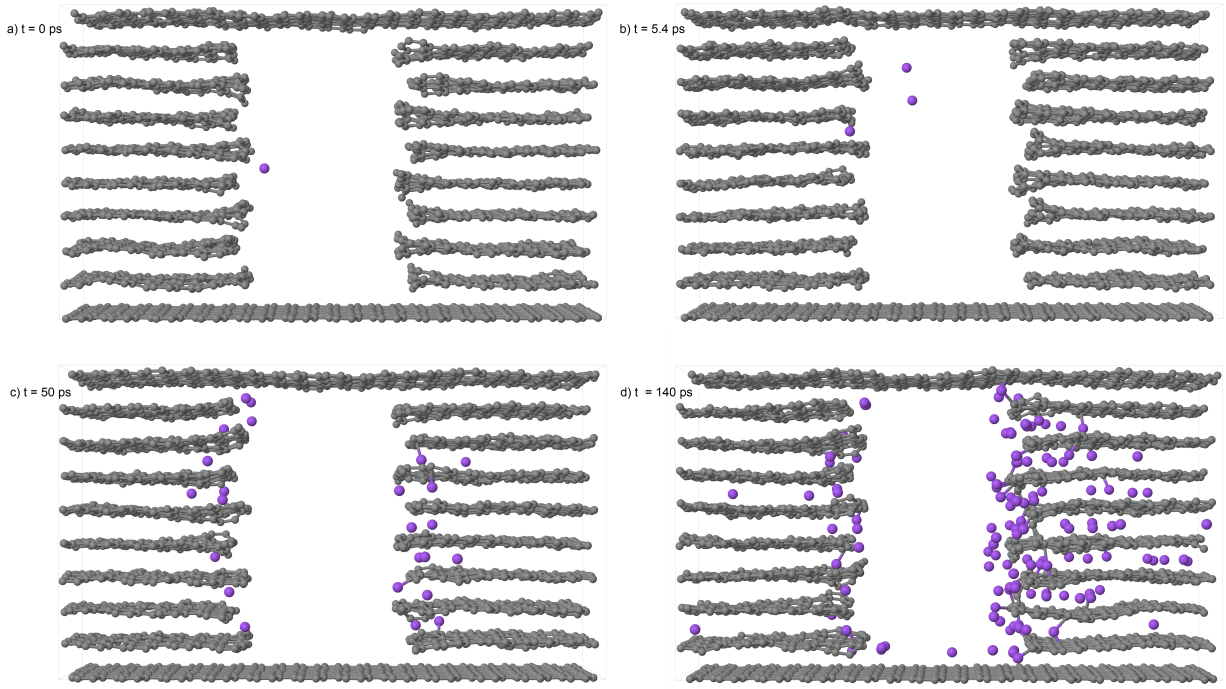

Figure 3.12: Snapshots of graphite slab with single and double defects exposed to sodium vapor of density 0.082 g/cm^3. The first three snapshots were during the temperature increase from 300 to 1200K.

3.2.6 Concluding remarks

An empirical reactive force field has been optimized to study sodium diffusion in graphitic carbon. The quality of the force field has been assessed by comparing the reproduced data and new predicted with that of DFT. The force field also has been applied in simulations, displaying the key features of sodium intrusion in graphitic carbon. Overall, the force field exhibits acceptable accuracy and precision. The most significant drawback of the optimized force field is the lack of correct description of atomic charges of intercalated and adsorbed sodium. The applied EEM method has shown to be insufficient in capturing the exact qualitative behaviors of the atomic charges predicted by MDC-q. An alternative method to the EEM available is the atom-condensed Kohn-Sham DFT approximated to second order (ACKS2) [35]. Furthermore, the obtained results suggest that some of the adopted parameters should be re-optimized in order to alleviate other drawbacks of the force field. In general, the presented force field does achieve the goal in describing the sodium-carbon interactions in some extent.

Chapter 4

Carbon materials

Carbon exists in various chemical and structural forms and is remarkable versatile. One one hand, crystalline and ordered phases such as graphene/graphite and diamond, exhibit an exceptional range of properties. On the other is the wide classes of disordered amorphous structures of carbon existing in a wide range of densities ranging from low-density, char-like carbon to high-density diamond-like and tetrahedral amorphous carbon, with diverse chemical features. In this chapter, the main carbon allotropes graphite and diamond are presented in brief, describing their representative structures, polytypes and properties. The majority of these sections are drawn from *Structure and Texture of Carbon Materials* by Michio [36]. Potential carbonaceous anode materials for sodium ion-battery is also described focusing only on the major funds and advances achieved so far.

Carbon is capable of forming various allotropes with diverse structures and properties due to its hybridization. With four electrons in the outermost 2s and 2p orbitals, carbon can have three different hybridization sp, sp^2 and sp^3 when forming chemical bonds with other atoms. The hybridized sp orbital is composed of two σ and two π bonds, the sp^2 of three σ and one π bonds, and the sp^3 involves four σ bonds. These hybridization give a variety of carbon allotropes, and mixing different types of hybridization expands the variety further.

4.1 Graphite

Carbon bonding with sp^2 hybridization gives rise to planar, aromatic carbons such as benzene, anthracene, etc. Extending these aromatics in two dimensions produces graphene sheet, which is the fundamental structural unit of graphite, fullerenes and carbon nanotubes. Graphite consists of several graphene sheets stacking on top of each other in a specific manner. It is the most stable form of carbon allotrope under standard conditions, and a density of 2.267 gcm^{-3}. Similar to simple graphene sheet, carbons atoms are bonded covalently in regular hexagons along layers. The layers are held together by the delocalized π electrons, resulting in weak, attractive van der Waals forces. This allows the layers to be cleaved easily, exhibiting a lubricating property.

Graphite can have various stacking arrangements, including ABAB (hexagonal), ABCABC (rhombohedral) and less commonly AAA. Layers with no evident stacking order is termed *turbostratic*. Hexagonal and rhom-

bohedral graphite are both low-temperature and pressure forms and display similar physical properties. In hexagonal graphite, the layers are stacked in translational ABAB sequence with an in-plane nearest neighbor distance of 1.421 Å and perpendicular interplane distance of 3.35 Å at room temperature. The hexagonal phase is thermodynamically stable, but can transform into rhombohedral by grinding processes. Weak disorder resulted from stacking faults is often observed in the hexagonal arrangement. This deviation leads to a small increase of graphite interlayer distance. The graphene layers become both uncorrelated with their neighbor and possess a mean finite size, in which case they are called turbostratic carbon/graphite.

Despite graphite being the most stable allotrope, many carbons do not transform into graphite even at 3000°C or above. Denoted as non-graphitizing carbons, these materials are hard and low density, with isotropic and microporous structure. In contrast, graphitizing carbon has a soft and non-porous structure with a relatively high density. It can be transformed into crystalline graphite by a heat treatment at temperature range 2000-3000°C. Non-graphitizing carbons, due to its high degree of microporosity, show a remarkably high internal surface area available for adsorption/diffusion and chemical reactions. When further activating these materials by mild oxidation with a gas or chemical, it results in activated carbon with enhanced adsorption properties. In literature, the terms *soft* and *hard* carbon is frequently used for graphitizing and non-graphitizing carbon, respectively, based on their physical properties. These terms are slightly deceptive and often avoided. However, these terms are frequently used to distinguish carbonaceous anode materials of sodium-ion battery.

Several studies have been dedicated to characterize the disordered structure of soft and hard carbon. Many structural models have been suggested, still the detailed structure at atomic is not fully understood [37] [38]. The carbon structure depends largely on the type of precursor chosen and the preparation method. A wide range of structures can be obtained, raising the difficultly to construct a universal model structure. In general, most models suggest that the disordered carbon is composed of two domains: carbon layers with graphene-like structure and nanosized micropores formed between the stacked carbon layers.The graphene layers often contain vacancy defects. Only a few layers are stacked together, with some sort of stacking faults extending the interlayer spacing.

4.2 Diamond

Diamond is a well-known allotrope of carbon for its hardness and high density. It has a three-dimensional structure, where each carbon atom is tetrahedrally bonded to four other atoms, forming strong covalent sp^3 bonds. The crystal structure is face-centered cubic with a density of 3.515 gcm^{-3}. Its tetrahedral structure accounts for its hardness and stability under pressure. Cubic diamond is the hardest material known. It can scratch any other materials and is therefore used as cutting and polishing tools in industry. As opposed to graphite, diamond is electrically insulating. Even so, cubic diamond is one of the best conductor of heat, conducting up to five times the amount that copper does. Another possible crystal arrangement of diamond is hexagonal, also known as Lonsdaleite. Its crystal structure is similar to those of hexagonal graphite, but the interplanar separation is slightly smaller and the carbon atoms adopt different site locations. Several properties of hexagonal diamond are still to be determined.

4.3 Amorphous diamond-like carbon

Amorphous carbon (a-C) characterizes a non-crystalline allotrope of carbon. Long-range periodicity is not attained, but some short-range order can be observed. Amorphous carbon can have any mixture of sp^3, sp^2 and sp bonds. It covers a wide range of materials, from sp^2 low density graphite-like carbon to more sp^3 diamond-like amorphous carbon, covering the density range $1.2 - 3.1$ gcm^{-3}. The latter class is described in further details. It is important distinguished between these two forms and other possible networks with an intermediate-range of disorder. The properties of amorphous carbon depend largely on the relative amount of sp^2 and sp^3 hybridized bonds, as well as the preparation method and the concentration of hydrogen.

Amorphous carbon structure with significant sp^3 bonding is called diamond-like carbon (DLC). The carbon atoms are tetrahedrally arranged, but adopted a random rotation opposed to diamond, resulting in dangling bonds that can be terminated with hydrogen. It is common to distinguish between highly sp^3 bonded *tetrahedral amorphous carbon* (ta-C), hydrogen-free or with minimum amount of hydrogen and *hydrogenated amorphous carbon* (a-C:H).

In general, DLC displays many of the unique properties of diamond such as mechanical hardness, high density, chemical inertness and optical transparency. As mentioned, the nature of these properties depends on the ratio of sp^2 and sp^3 bonds, hydrogen concentration and preparation conditions. Consisting mostly of sp^3 bonding ta-C has a very high atomic density similar to diamond (~ 3.1 gcm^{-3}), while a-C:H has a lower value (1.2 - 2.2 gcm^{-3}). The same characteristic gives ta-C an extremely high strength and hardness. In contrast, a-C:H exhibits a lower modulus because hydrogen bonding reduces the mean carbon-carbon coordination. Diamond has the largest room temperature thermal conductivity. This particular property is lacking in DLCs due to the atom disorder scatting phonons. ta-C does have high thermal conductivity, though not comparable with that of crystalline solids. The variations in properties make ta-C and a-C:H suitable for different applications. The lower atomic density of a-C:H films is appropriate used as diffusion barriers in electronic and food packaging. The high hardness of ta-C is more suitable for wear-resistant protective coatings such as optical windows, car parts and microelectro-mechanical devices.

4.4 Carbonaceous anode materials for NIBs

Rechargeable lithium-ion batteries (LIBs) are considered as the most successful and sophisticated energy storage devices. Originally developed for applications in portable electronic devices, large-scale LIBs are now used as high-energy and safe power sources in electric cars. Furthermore, LIBs have been suggested and tested as an electric energy storage (EES) to efficiently store generated electrical energy in power grids [39, 40]. The increasing demand of these markets have indeed raised the cost of LIBs. Contributing to this high cost is the limited lithium resources that are geographically constrained. In contrast, sodium resources are unlimited and widely distributed. Based on the similar alkali metal chemistries as in LIBs and the availability of sodium, sodium-ion batteries (LIBs) emerge as a promising alternative to LIBs.

While LIB technology is well-established, the current research on NIB is still in its early stage. Since lithium and sodium are alkali metals, they share similar chemical properties such as ionicity, electronegativity and electrochemical reactivity. Research on sodium-ion batteries can be conducted based on previously applied materials and methods in the lithium counterpart. Nevertheless, there are fundamentals differences between

the two elements that influence the thermodynamic and kinetic properties of NIBs [41]. Sodium atom is three times heavier than lithium atom, which makes NIBs slightly heavier than their analogues LIBs. The larger ionic radius of sodium makes it even more reactive with the organic electrolyte solvents. Besides, the larger size of Na^+ also requires the host electrode material to have sufficiently large channels and interstitial space to rapidly insert and extract sodium ions. Sodium metal has a considerable lower melting temperature compared to lithium metal, which is a drawback related to short circuits (dendrite formation) and safety issues when used as anode for NIBs operated at ambient temperature. Additionally, metallic sodium exhibits low energy density and output voltage as opposed to metallic lithium [1]. Sodium is less reducing than lithium (-2.71 V compared to -3.04 V), and the gravimetric capacity is lower (1165 g^{-1} compared to 3829 g^{-1}).

One major challenge in developing NIB still is the lack of a suitable negative electrode. In LIBs, graphite is the commonly used anode material due to its high reversible capacity and stability. Graphite anodes can yield a reversible capacity of 360 mAh g^{-1}, approaching to the theoretical value of 372 mAh g^{-1}. When electrochemically reduced, Li^{+1} are easily inserted/intercalated between the graphite layers, and Li-graphite intercalation compound (GIC) is formed with stage transformations. At the first stage (stage-I), the graphite layers are completely filled with Li-ions, yielding LiC_6. Unfortunately, graphite anodes are unsuitable as they are less electrochemically active in Na cells [42, 43]. Only a small amount of sodium intercalates into graphite under the condition of high temperature. Besides, computational studies calculate a positive intercalation energies, suggesting that sodium insertion in graphite is thermodynamically unfavorable [39] [44]. Sodium atoms seem to prefer to cluster rather than to intercalate into the crystalline phase. In contrast, non-graphitizable carbons with a lower crystalline structure, such as soft and hard carbon based anodes, are more electrochemically active in Na cells. Their properties are discussed further in a general aspect. Carbonaceous anode materials can be prepared from different precursors and conditions, showing slightly different properties.

Soft carbon anodes when applied in Li cell, exhibit a high reversible capacity and good rate performance. However, a large irreversible capacity is observed during the initial cycle due to the electrolyte decomposition and dendrite formation on the surface of the anode. They are generally considered as a poor choice. The turning point is the study performed by Doeff *et al.* [43] which reported the reversible sodium insertion/extraction of soft carbon anodes forming NaC_{24}. The reversible capacity delivered was relatively higher (90 mAh g^{-1}), though the Na cells were operated at higher temperature (86 °C). A recent study shows that liquid decomposition and dendrite growth can be avoided if the precursor is carefully chosen and prepared at certain conditions [45]. They also reveal the relationship between the high reversible capacity and the increased interlayer spacing upon sodium insertion, and justify that irreversible initial capacity is due to the irreversible part of the interlayer expansion.

Hard carbon was the anode material used in the first commercial LIB. Lithium atoms are inserted in the structure without the formation of a staging transition due to the structural disorder. Hard carbon anodes in Li cells are reported to deliver a reversible capacity that exceeds the theoretical analogue of graphite, even though the volumetric capacity is lower than that of graphite. Stevens and Dahn were the first to report a relatively high electrochemical reversibility of sodium at room temperature [46]. The hard carbon anodes delivered about 300 mAh g^{-1} but the cycle stability was not sufficient. The high reversible capacity and the underlying insertion mechanisms can be explained by the charge/discharge profile of hard carbon anode [2]. The profile displays an irreversible plateau at very potential for the initial insertion process, identifying

a small dendrite formation on the surface. An inclined region is then observed that slowly decays from 1.2 to 0.1 V during the insertion process, followed with a long plateau region around 0.1 V, reaching the reversible capacity of 300 mAh g^{-1}. The sloping region can be ascribed to sodium intercalates into interlayer spacings of graphene sheets, and the low potential plateau indicates further diffusion into micropores [47, 48]. When extracting sodium, the potential is observed near 0.1 V with reversible capacity around 120 mAh g^{-1} before gradually increases to 1.2 V demonstrating a reversible sodium insertion for hard carbon. Although the low potential makes hard carbon energetically favorable, it raises safety concerns of dendrite formation when high current densities are used. This can be diminish considerably with appropriate electrolyte and additives.

Contrary to graphite, amorphous carbon (a-C) with highly disordered structure has shown to efficiently insert Na. Amorphous carbon coated with sodium fluorinated iron phosphate ($Na_7Fe_7(PO_4)_6F_3$) studied experimentally displayed moderate reversible capacity at high current rate [49]. Computational studies at atomistic level have discovered that amorphization of a silicon framework remarkably improves the interaction of Na [50, 51]. Based on this observation, Legrain and his co-workers performed a combined *ab initio* computational and experimental study to investigate the effect of amorphization of carbon on the insertion of Li and Na [3]. The computational results revealed several possible insertion sites for Na in amorphous carbon, with half of them showing strong binding energies. This shows that amorphization makes Na insertion thermodynamically favored, promising a-C as a potential anode material. Motivated by this study of Legrain, a-C models with the same density is generated in this thesis work, though with a larger system size. The *ab initio* method used by Legrain is thus prohibited due to the increased system size, and empirical force field appears to be a more suitable choice.

Chapter 5

Computational details

5.1 Molecular dynamics simulation

Molecular dynamics (MD) simulation was applied in conjunction with the previously optimized ReaxFF$_{\mathrm{NaC}}$. All simulations were performed in the simulator program LAMMPS using the version of ReaxFF implemented in C. A script of the simulation is attached in Appendix B.

A cubic cell of size $10 \times 10 \times 10$ (Å^3) contained 125 carbon atoms that was randomly placed. The cell was kept fixed throughout the simulation process. Periodic boundary conditions were applied in all directions to keep the number of particles constant and cancel the boundary effect. Using the Nose-Hoover thermostat [34], the cell was then subjected to the liquid quench routine performing in the canonical ensemble (NVT). A small time-step of 0.01 fs was chosen to ensure proper energy conservation at high temperatures. As the initial configuration of the system was constructed by randomly placing the carbon atom, various amorphous structures were obtained for the same density. For this reason, the radial distribution function (RDF) of the generated structures were compared with the experimental neutral scattering data from Ref. [6]. Structures giving a good fit were further subjected to sodium insertion at 300 K. A vacuum void of 10 Å was created above the amorphous structure, where the sodium atoms were randomly distributed. Two different densities of sodium were simulated with the initial velocity assigned according to the Boltzmann distribution of 300 K. RDF and the angel distribution function were applied to characterize the atomistic structure of the resulting amorphous structures inserted with sodium.

5.2 Liquid quench routine

The initial computational steps were dedicated to generate highly disordered amorphous carbon models. The liquid quench routine was executed according to Rangananthan *et al.* [52]. In the overall process, the steps involved were as followed:
1) N carbon atoms are distributed randomly in the simulation box.
2) The temperature is ramped up to 10000K followed by an equilibration of the system at this temperature.
3) The system is then quenched to 3000 K.

4) The system is annealed at 3000 K.
5) Finally, the system is quenched and equilibrated at 300 K.

The overall procedure above is summarized schematically in Table 5.1, including the timescales performed for each step. The density was set to 2.5 gcm^{-3}, close to the previously reported value of amorphous carbon [6]. The achieved structures from liquid quench depend largely on the quenching rate. Ishimaru and co-workers suggested from their study with amorphous silica a cooling rate threshold below 10^{12}K/s to recover the amorphous network [5]. The quenching rates simulations were therefore preserved within the range $1.5 - 3.0 \times 10^{11}$ K/s.

Table 5.1: Liquid quench simulation process to create amorphous carbon.

Step	Simulation procedure	Timescales [ps]
1	Distribute N carbon atoms randomly	-
2	Ramp temperature to 10000K and equilibrate at	10
3	Quench to 3000 K	20
4	Anneal at 3000 K	10
5	Quench to and anneal at 300 K	20
6	Sodium insertion at 300 K	10

5.3 Radial distribution function

Radial distribution function (RDF) is computed with the program *Interactive Structure Analysis of Amorphous and Crystalline Systems* (ISAACS) [53]. It is specially developed to study structural characteristics of crystalline and amorphous systems. The angle distribution function is also computed with the program.

Radial distribution function denoted $g(r)$ defines the probability of finding a particle in distance r from a reference particle [10]. RDF is a useful tool to describe the atomic structure of a system and varies greatly for gases, liquids and solids. In a solid, the RDF typically has an infinite number of sharp peaks, in which the separations and heights describe the lattice. For a liquid, the RDF is intermediate between the solid and the gas, consisting of a small number of peaks as short distances that steadily decays to a constant value at longer distances.

Considering a spherical shell with radius r and thickness δr, its volume is written as [53]:

$$V_{shell} = \frac{4}{3}\pi(r+\delta r)^3 - \frac{4}{3}\pi r^3 \simeq 4\pi r^2 \delta r. \tag{5.1}$$

The radial distribution function is simply the ratio of density of atoms at the distance r by overall density:

$$g(r) = \frac{\rho(r)}{\rho} \quad \rho = \frac{N}{V}, \tag{5.2}$$

where $\rho(r)$ is the local density of atoms as function of radius. N is the total number of atoms in the system, and V is the total volume. Defined N_r as the average number of particles at the distance between r and $r + dr$, the radial distribution function is then expressed as:

$$g(r) = \frac{N_r}{V_{shell}} \frac{1}{\rho}. \tag{5.3}$$

In this way, the RDF provides information about the density of atoms at a given radius r and measures distance of particles to their neighbors, averaging over large number of atoms. In some cases, the reduced radial distribution function is computed. It is expressed as:

$$G(r) = 4\pi r \rho_0 \tilde{g}(r), \tag{5.4}$$

where $\tilde{g}(r) = g(r) - 1$. In cases with more than one type of atoms, a partial RFD for each type can be computed according to:

$$g_{\alpha\beta}(r) = \frac{N_{r,\alpha\beta}}{V_{shell}} \frac{1}{\rho_\alpha}. \tag{5.5}$$

Radial distribution function is an effective way to describe how the atoms on average are radially packed around each other. Thus, RDF reveals important details about the atomic structure of the system being studied.

Chapter 6

Results and discussion

6.1 Amorphous carbon structures

Radial distribution function is computed for the five amorphous carbon structures obtained from the liquid quench process. These RDFs are compared with the neutron-diffraction data from Ref. [6] to ensure an appropriate atomic structure. Fig. 6.1a shows the RDFs of the generated a-C structures. Clearly, there is an negligible variation in the G(r) for each structure, implying that the generated models are similar in structure. The successive discrete peaks correspond to the average nearest-neighbor distances, i.e. the first peak corresponds to the nearest neighbor shell, the second peak to the second nearest neighbor shell, and so on. The first sharp peak occurs roughly at 1.44 Å, which is very close to the carbon-carbon bond length in graphite (1.42Å). The second peak falls at 2.5 Å, also very near the lattice parameter a (the shortest distance between the outermost carbons forming a 120° C-C-C) of graphite (2.46 Å). These peaks indicate that the amorphous structures contain a large fraction of sp^2 bonds, with a small fraction of sp^3 because the peaks are also broadened. High fraction of sp^2 bonds suggests that carbon atoms are fused in rings, more specifically six-membered rings. To confirm this, the angle distribution functions of these a-Cs are computed and displayed in Fig. 6.1b. The bond angle ranges from ∼100° to 140° with a peak at 120°. Thus, the generated amorphous structures are composed of mostly six-membered rings, and a small fraction of five- and seven-membered rings. The small peak at 60° indicates the occurrence of three-membered rings.

Out of the five generated structure, two of these give a good fit of the RDF to the experimental RDF, shown in Fig. 6.2. The corresponding structures are displayed in Fig. 6.3. Although with some minor deviations, the RDFs of these show a similar shape and exhibit distinct peaks at similar separation distances to the experimental one. They are also in good agreement with the additional RDF of an amorphous structure obtained by DFT [3]. The resulting amorphous carbon structures contain a high fraction of six-membered rings with no short-range order.

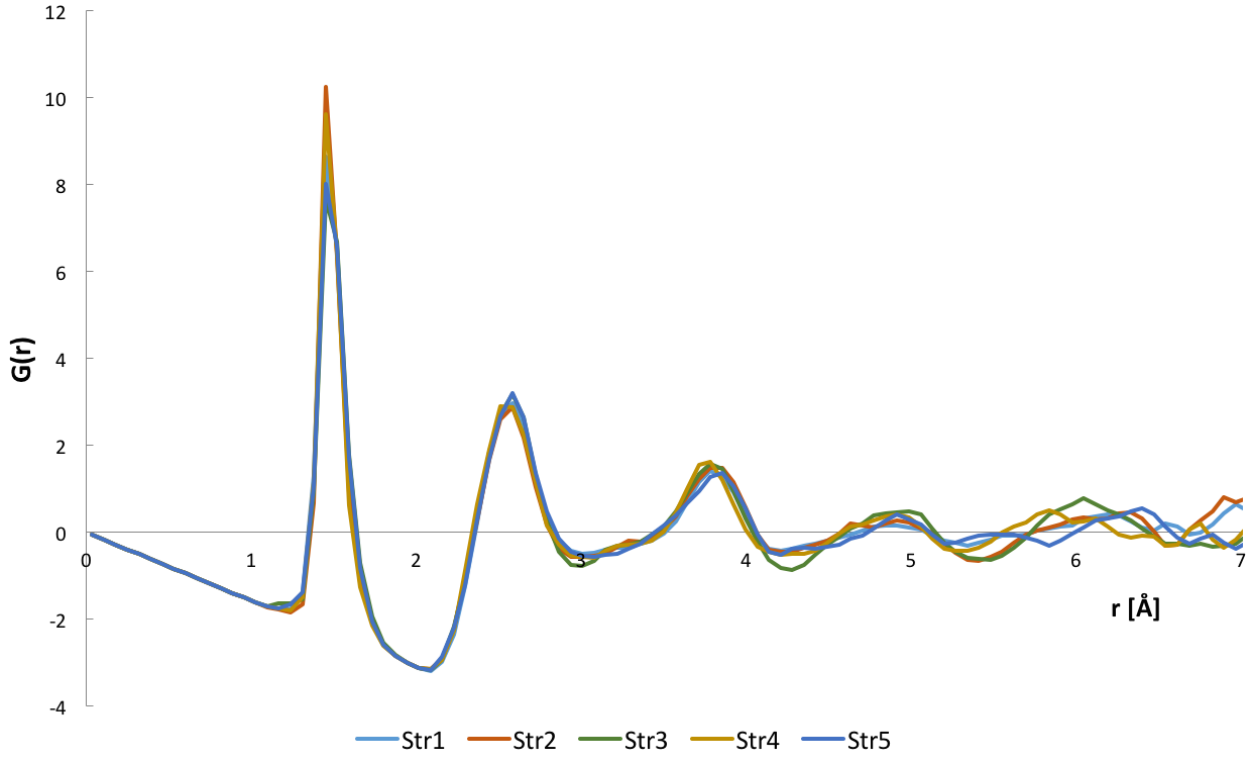

(a) RDFs of generated amorphous carbon structures.

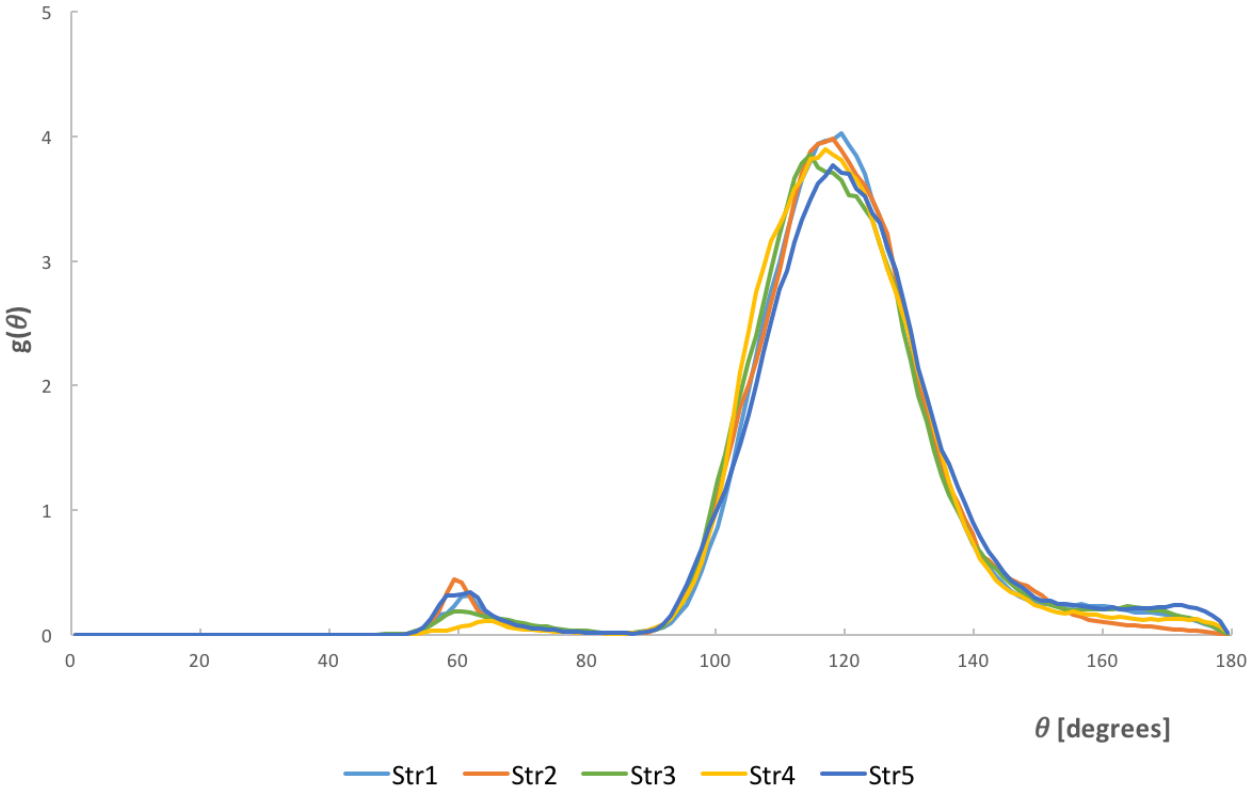

(b) Angle distribution functions of generated amorphous structures.

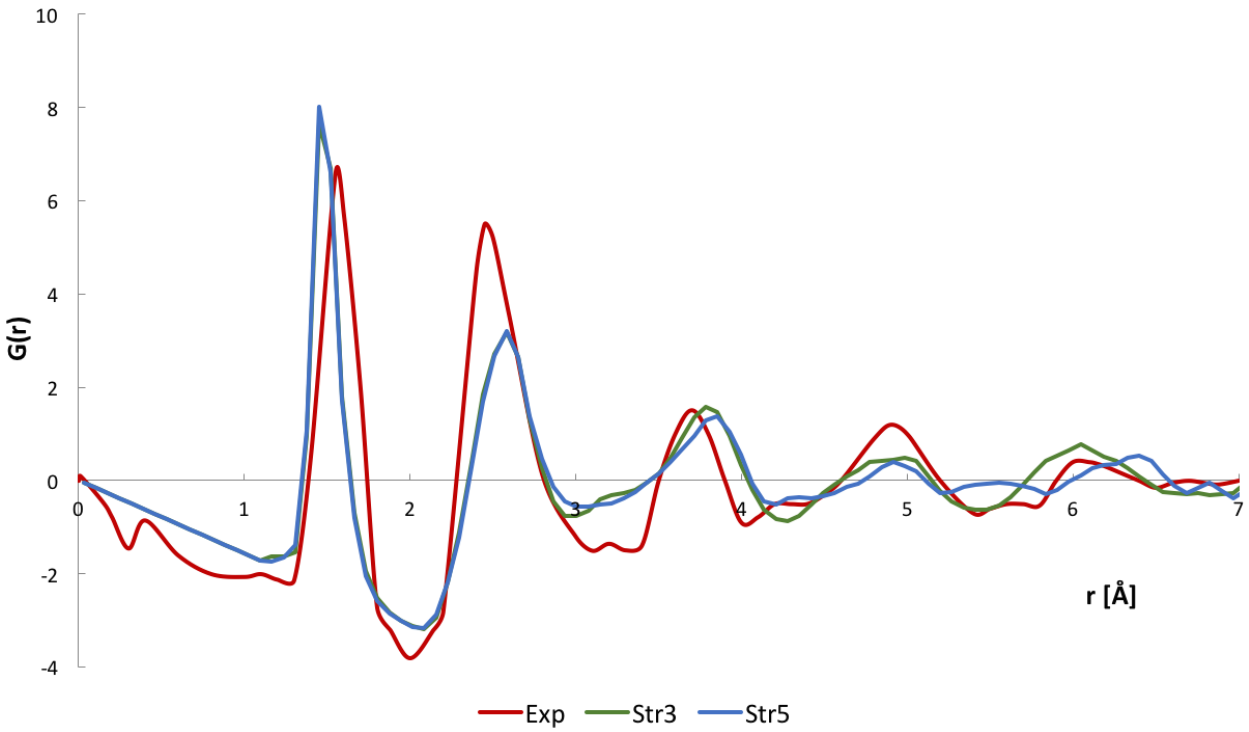

Figure 6.2: Respective RDFs of structure 3 and 5 together with the experimental data [6].

6.2 Sodium insertion

The two a-C structures displayed Fig 6.3 are subjected to sodium insertion at 300 K. The same simulation processes have been performed for both structures. Comparing the individual simulations, very similar features are observed. For this reason only one of them is discussed to show the details.

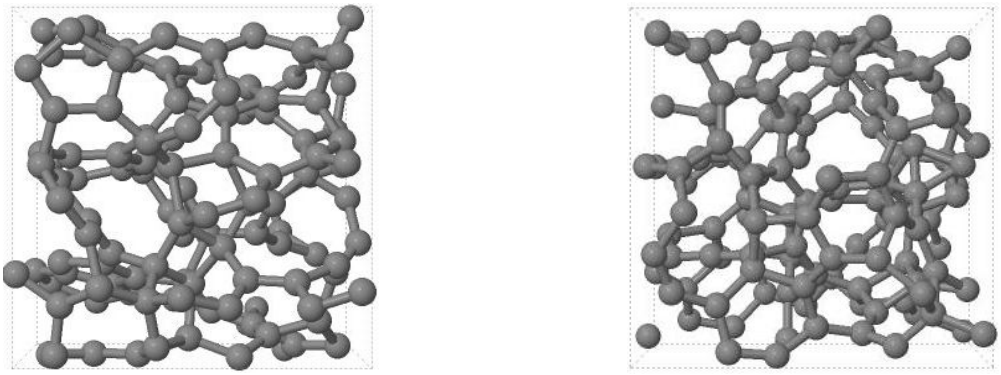

(a) (b)

Figure 6.3: The resulting amorphous carbon structures, Str3 and Str5, respectively.

Fig 6.5 shows snapshots taken from the simulation of the a-C structure exposed to sodium of density 0.043 gcm^{-3}. This corresponds to 21 sodium atoms per unit cell. Soon after the simulation has began, some of the freely Na atoms in the vacuum top immediately adsorb on the surfaces of the a-C. Seen in Fig. 6.5b, some Na atoms are attracted on the surface, even a few are entering the a-C structure. After 13 ps all sodium atoms

are completely adsorbed on the surfaces, searching for available insertion sites. However, during this time more Na atoms have entered the carbon structure, accommodating the insertion sites with the lowest energy barrier. Subsequent insertion is thus inhibited. For the remaining simulation, the entered Na atoms do not diffuse further into the a-C structure and remain at their respective sites. In addition, the a-C structure is expanded upon sodium insertion. This is confirmed by the partial RDF for carbon shown in Fig. 6.4, in which the original peaks have been broadened. The first peak of the RDF for a-CNa falls at 1.475 Å, showing an increase of 0.3 Å from the original distance (1.449 Å). These broadened peaks suggest a change in bonding to a more sp^3 character [52].

Increasing the density to 0.085 gcm^{-3}, similar features as the case with lower density are also observed. Fig. 6.6 shows the snapshots taken from the simulation. Almost immediately, Na atoms quickly adsorb on the carbon surface. As there are twice as many Na atoms in the same unit cell, a higher pressure is exerted on the a-C structure, effectively pushing the Na atoms towards the structure. Already at 2 ps, shown in Fig. 6.6b, several Na atoms have been inserted, expanding the a-C structure. Further in the simulation, Na atoms progressively enter the structure, overcoming the higher insertion barriers. After about 30 ps the system begins to stabilize. Evidently, the final a-C has expanded in greater extent, compared to that of lower density, with more Na atoms further inside the structure. Above this density, the pressure is too high and deteriorate the a-carbon structure.

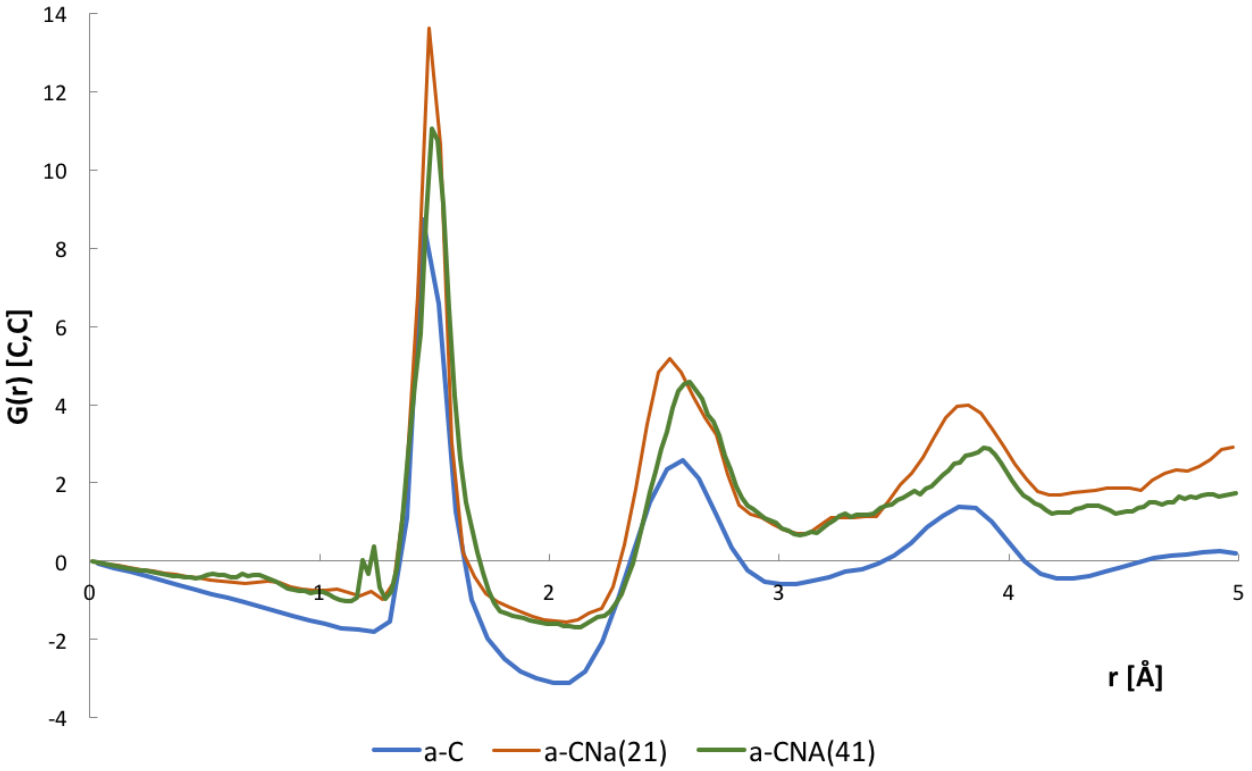

Figure 6.4: Compared RDF of initial generated a-C structure and the same carbon structure with 21 and 41 Na atoms, respectively.

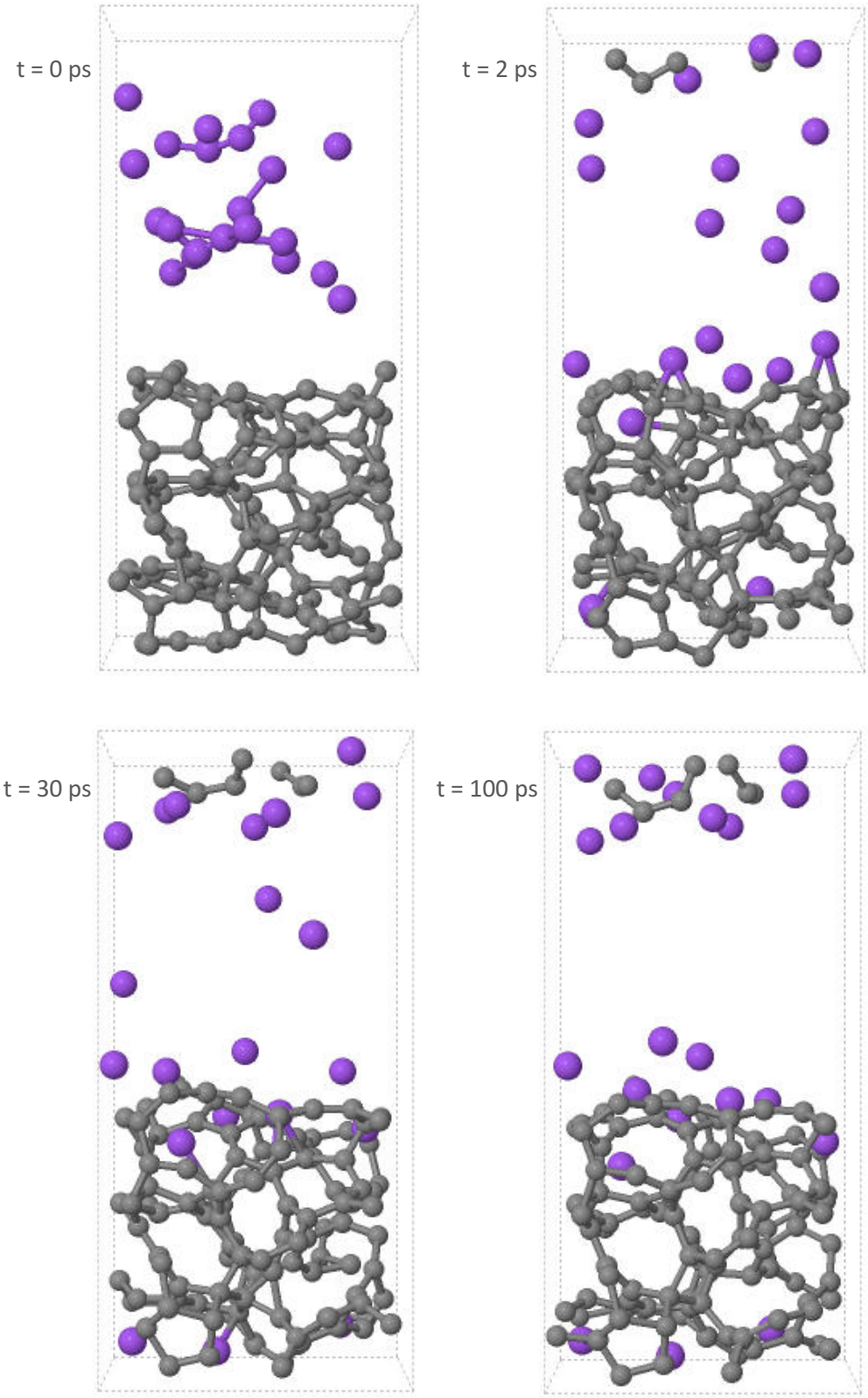

Figure 6.5: Snapshots of sodium insertion into the generated amorphous carbon structure. The density of sodium is 0.043 gcm^{-3}.

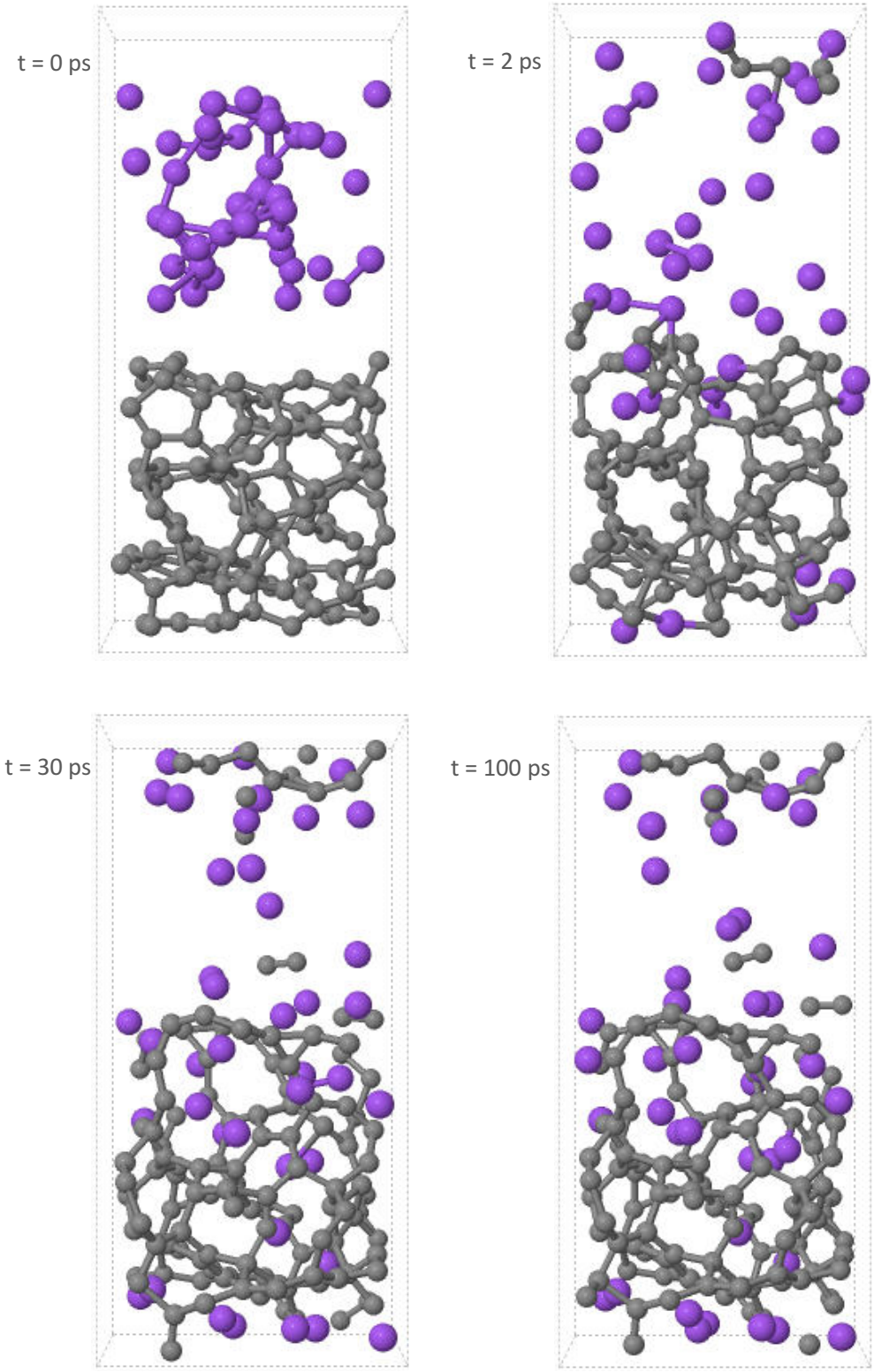

Figure 6.6: Snapshots of sodium insertion into the generated amorphous carbon structure with a density 0.085 gcm^{-3}.

The amorphous carbon containing sodium atoms of different densities have alternated their initial structures. To give an indication about their atomic structure afterwards, the total RDFs for each structure are shown in Fig. 6.7, with high density referring to 0.085 gcm^{-3} and low density to 0.043 gcm^{-3}. The total RDF is computed as a weighted sum of the respective partial RDFs [53]. As seen, both RDF displayed a prominent peak at distance ∼2.3 Å, indicating this distance as the particular favorite separation distance for the carbon neighbors and sodium atoms. For the case of low density, where the a-C structure does not expand considerably as only few Na atoms have been inserted, the peak is higher and sharper.

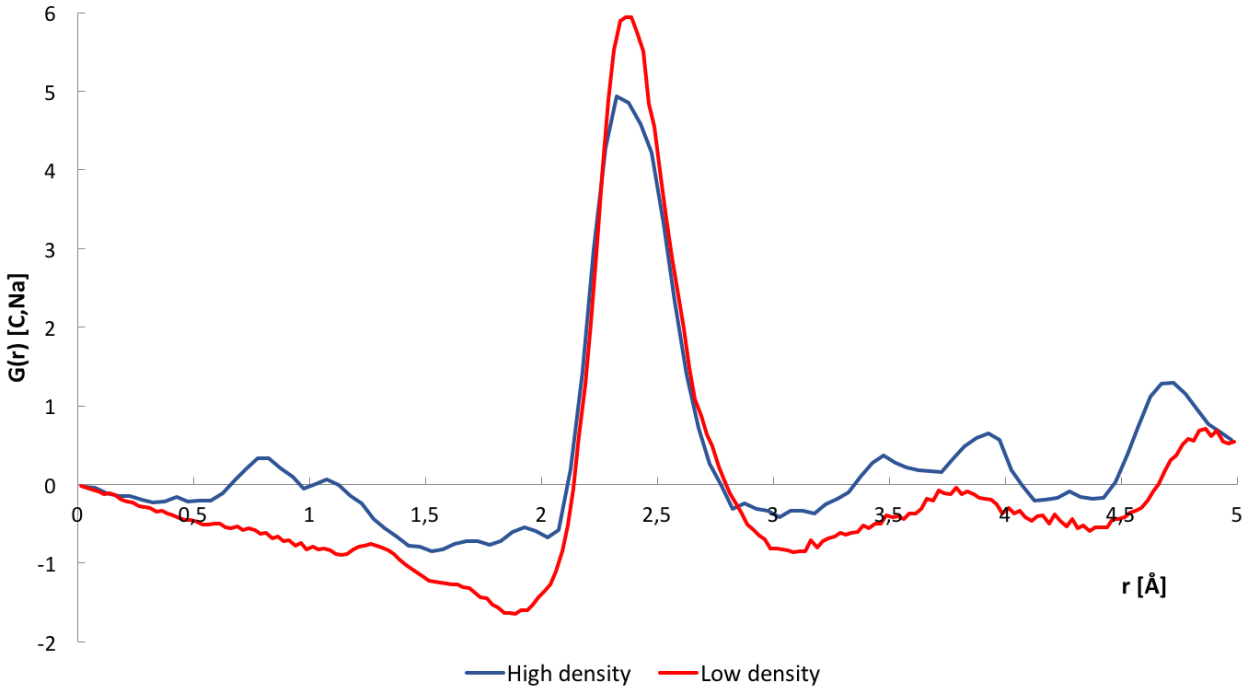

Figure 6.7: Total RDFs of amorphous carbon structures with sodium density 0.085 gcm^{-3} (high density) and with 0.043 gcm^{-3} (low density), respectively.

6.3 Comments to the force field

The objective of this thesis is to apply the optimized reactive force field in simulations of sodium insertion in amorphous structure of carbon. In this way, the force field can be qualitatively investigated in studying a different carbon structure and sodium diffusion at room temperature.

Several parameters in the force field have been adopted from other set of relevant studies. The parameters for carbon are adopted consistently from the work of Raju et al. [21], where they have been successfully modeled lithium interaction in various forms of highly crystalline carbon. In this work, the process of generating amorphous structures depends entirely on these adopted parameters and the quality of these. Results from the MD simulations indicate that these parameters are capable of constructing amorphous structures with a reasonable accuracy. This suggests that other allotropes of carbon can be modeled using this set, however it relies generally on the further interactions/applications of interest. Other set of parameters for pure carbon that have been developed [11, 54]. The reason the particular set from Raju are adopted because of the simi-

larities between the alkali lithium-carbon and sodium-carbon system. The optimized force field qualitatively simulated sodium interaction in generated amorphous structure and displayed reasonable results. In order to genuinely evaluate the quality of the force field more work is required. Overall, these simulation results demonstrate that the force field is able to qualitatively describe relevant sodium interactions in other carbon allotropes.

Chapter 7

Conclusion

Sodium intrusion in carbon cathodes can cause serious damage to the aluminum electrolysis cell. It is thus important to study the sodium intrusion mechanism and possible diffusion paths on the atomic scale. As *ab inito* methods becomes computationally costly for large system sizes and time scales, more approximate force field methods are required. An empirical reactive force field has been developed to study sodium interaction in graphitic carbon [4]. The force field has been trained against a set of relevant geometries, potential energy surfaces and charge transfer calculated with density functional theory. The optimized force field reproduces the training data and predict new data with moderate accuracy. The most considerable setback is the charge transfer determined by the EEM method. EEM is unable to capture the atomic charge behavior of intercalated and adsorbed sodium to graphite, respectively. The force field has been applied in hybrid grand canonical MC/MD simulations of sodium intrusion graphite. A double vacancy defect in a graphene layer is large enough for sodium to enter the structure, and effectively shift the stacking order of graphene layers that it accommodate in between. In a porous graphite structure, sodium atoms are quickly intercalated into the open channels between the graphene layers until the structure is completely saturated. Although the force field display some short-comings compared with results derived from DFT, its overall accuracy and precision are satisfactory.

Sodium diffusion into graphitic and non-graphitic carbon have also been studied in the field of sodium ion battery. Graphite anodes have proved to be inadequate for battery applications as the reversible capacity is too low. Amorphous carbon has emerged to be a more appropriate choice. Results from a computational study indicates that amorphous carbon provides several possible insertion sites with low energy barrier, making sodium insertion thermodynamically favored [3]. In this thesis, the optimized force field is applied in simulations to qualitatively study sodium insertion in amorphous carbon at room temperature. The amorphous structures generated from the liquid-quench method display similar structural features reported in literature. The structures contains mostly the thermodynamically stable six-membered rings that are highly distorted. Small fraction of five- and seven-membered rings also occurs. The force field is able to generate amorphous carbon structure with moderate precision. The process of constructing amorphous structure depends entirely on the parameters for carbon and hydrogen and the optimized quality of these. These parameters adopted from the work of Raju et al. [21] due to the similarities between lithium- and sodium-carbon systems studied. Sodium atoms of two different densities are subsequently inserted into two

of the amorphous structures, and similar behaviors are observed. In the case of low density, only a small amount of sodium is inserted into the structure, occupying the insert sites of lowest energy. At higher density, the sodium atoms exert a higher pressure on the carbon structure. More sodium atoms are able to enter the structure through the insertion sites of higher energy. These simulation results demonstrate that the force field is able to qualitatively describe sodium diffusion into amorphous carbon.

The presented work in this thesis can be regarded as a preliminary study of sodium diffusion in amorphous carbon using the developed force field. The obtained results qualitatively suggest that the force field is capable of describing relevant sodium interactions in other carbon allotropes and even at another temperature. The sodium-ion research field is an obvious application area of the force field, presenting a vast number of possible sodium-carbon systems to be studied. In this work, sodium atoms have only inserted in the carbon structure, it could be interesting to remove the inserted sodium atoms, mimicking the reversible de/insertion reaction in batteries. In doing so, important properties such as reversible capacity and diffusion coefficient can be calculated. Prior for further applications, the force field must be re-optimized considering the inaccurate description of the charge transfer provided by the EEM method. Some of the adopted parameters can also be re-optimized to increase the overall accuracy. In conclusion, the optimized force field displays a moderate adaptability and can be further optimized for specific applications.

Bibliography

[1] M. D. Slater, D. Kim, E. Lee, and C. S. Johnson, "Sodium-ion batteries," *Advanced Functional Materials*, vol. 23, no. 8, pp. 947–958, 2013.

[2] M. Dahbi, N. Yabuuchi, K. Kubota, K. Tokiwa, and S. Komaba, "Negative electrodes for Na-ion batteries.," *Physical chemistry chemical physics : PCCP*, vol. 16, no. 29, pp. 15007–15028, 2014.

[3] F. Legrain, J. Sottmann, K. Kotsis, S. Gorantla, S. Sartori, and S. Manzhos, "Amorphous (Glassy) carbon, a promising material for sodium ion battery anodes: A combined first-principles and experimental study," *Journal of Physical Chemistry C*, vol. 119, no. 24, pp. 13496–13501, 2015.

[4] E. Hjertenaes, A. Q. Nguyen, and H. Koch, "A ReaxFF force field for sodium intrusion in graphitic cathodes," *Phys. Chem. Chem. Phys*, pp. 31431–31440, 2016.

[5] M. Ishimaru, S. Munetoh, and T. Motooka, "Generation of amorphous silicon structures by rapid quenching: A molecular-dynamics study," *Physical Review B*, vol. 56, no. 23, pp. 15133–15138, 1997.

[6] K. W. R. Gilkes, P. H. Gaskell, and J. Robertson, "Comparison of neutron-scattering data for tetrahedral amorphous carbon with structural models," *Physical Review B*, vol. 51, no. 18, pp. 12303–12312, 1995.

[7] A. Szabo and N. S. Ostlund, *Modern Quantum Chemistry: Introduction to Advanced Electronic Structure Theory*. Dover Books on Chemistry, Dover Publications, 1989.

[8] P. Atkins and R. Friedman, *Molecular Quantum Mechanics*. Oxford University Press, 2010.

[9] T. H. Dunning Jr, "Gaussian basis sets for use in correlated molecular calculations. I. The atoms boron through neon and hydrogen," *J. Chem. Phys.*, vol. 90, no. 1989, p. 1007, 1989.

[10] A. R. Leach, *Molecular modelling: principles and applications*. Pearson education, 2001.

[11] A. C. T. van Duin, S. Dasgupta, F. Lorant, and W. A. Goddard III, "ReaxFF: A Reactive Force Field for Hydrocarbons," *J. Phys. Chem. A*, vol. 105, pp. 9396–9409, 2001.

[12] T. P. Senftle, S. Hong, M. M. Islam, S. B. Kylasaf, Y. Zheng, Y. K. Shin, C. Junkermeier, R. Engel-Herbert, M. J. Janik, H. M. Aktulga, T. Verstraelen, A. Grama, and A. C. T. van Duin, "The ReaxFF Reactive Force-field: Development, Applications, and Future Directions," *npj Computational Materials*, vol. 2, p. 15011, 2016.

[13] M. F. Russo and A. C. T. Van Duin, "Atomistic-scale simulations of chemical reactions: Bridging from quantum chemistry to engineering," *Nuclear Instruments and Methods in Physics Research, Section B: Beam Interactions with Materials and Atoms*, vol. 269, no. 14, pp. 1549–1554, 2011.

[14] A. C. T. van Duin, A. Strachan, S. Stewman, Q. Zhang, X. Xu, and W. A. Goddard III, "ReaxFF SiO Reactive Force Field for Silicon and Silicon Oxide Systems," *Journal of Physical Chemistry A*, vol. 107, no. 19, pp. 3803–3811, 2003.

[15] E. de Vos Burchart, V. A. Verheij, H. van Bekkum, and B. van de Graaf, "A consistent molecular mechanics force field for all-silica zeolites," *Zeolites*, vol. 12, no. 2, pp. 183–189, 1992.

[16] S. Goverapet Srinivasan, A. C. T. Van Duin, and P. Ganesh, "Development of a ReaxFF potential for carbon condensed phases and its application to the thermal fragmentation of a large fullerene," *Journal of Physical Chemistry A*, vol. 119, no. 4, pp. 571–580, 2015.

[17] W. J. Mortier, K. Van Genechten, and J. Gasteiger, "Electronegativity equalization: application and parametrization," *Journal of the American Chemical Society*, vol. 107, no. 4, pp. 829–835, 1985.

[18] A. K. Rappé and W. A. Goddard III, "Charge Equilibration for Molecular Dynamics Simulations," *Journal of Physical Chemistry*, vol. 95, no. 8340, pp. 3358–3363, 1991.

[19] R. T. Sanderson, "Partial Charges on Atoms in Organic Compounds," *Science*, vol. 121, no. 3137, pp. 207–208, 1955.

[20] A. Jaramillo-Botero, Q. An, P. L. Theofanis, and W. A. Goddard, "Large-scale molecular simulations of hypervelocity impact of materials," *Procedia Engineering*, vol. 58, pp. 167–176, 2013.

[21] M. Raju, P. Ganesh, P. R. C. Kent, and A. C. T. Van Duin, "Reactive force field study of Li/C systems for electrical energy storage," *Journal of Chemical Theory and Computation*, vol. 11, no. 5, pp. 2156–2166, 2015.

[22] J. G. O. Ojwang, R. A. van Santen, G. J. Kramer, A. C. T. van Duin, and W. A. Goddard III, "Modeling the sorption dynamics of NaH using a reactive force field.," *The Journal of chemical physics*, vol. 128, p. 164714, 2008.

[23] J. P. Perdew, K. Burke, and M. Ernzerhof, "Generalized Gradient Approximation Made Simple," *Physical Review Letters*, vol. 77, no. 18, pp. 3865–3868, 1996.

[24] J. Louwen and E. Vogt, "Semi-empirical atomic charges for use in computational chemistry of molecular sieves," *Journal of Molecular Catalysis A: Chemical*, vol. 134, no. 1-3, pp. 63–77, 1998.

[25] ADF, "ReaxFF Manual," pp. 1–20, 2014.

[26] E. Iype, M. Hütter, A. P. J. Jansen, S. V. Nedea, and C. C. M. Rindt, "Parameterization of a reactive force field using a monte carlo algorithm," *Journal of Computational Chemistry*, vol. 34, no. 13, pp. 1143–1154, 2013.

[27] W. J. Mortier, S. K. Ghosh, and S. Shankar, "Electronegativity-equalization method for the calculation of atomic charges in molecules," *Journal of the American Chemical Society*, vol. 108, no. 15, pp. 4315–4320, 1986.

[28] M. Swart, P. T. Van Duijnen, and J. G. Snijders, "A Charge Analysis Derived from an Atomic Multipole Expansion," *Journal of Computational Chemistry*, vol. 22, no. 1, pp. 79–88, 2001.

[29] P.-c. Tsai, S.-C. Chung, S.-k. Lin, and A. Yamada, "Ab initio study of sodium intercalation into disordered carbon," *Journal of Materials Chemistry A*, vol. 3, no. 18, pp. 9763–9768, 2015.

[30] A. N. Rosli, I. F. Wahab, N. A. Zabidi, and H. A. Kassim, "The Study of Band Structure of Graphite Intercalation Compound Containing Sodium Calculated Using Density Functional Theory," in *Journal of Physics: Conference Series*, vol. 622, p. 12049, IOP Publishing, 2015.

[31] W. Wan and H. Wang, "Study on the first-principles calculations of graphite intercalated by alkali metal (Li, Na, K)," *Int. J. Electrochem. Sci*, vol. 10, pp. 3177–3184, 2015.

[32] T. P. Senftle, R. J. Meyer, M. J. Janik, and A. C. T. Van Duin, "Development of a ReaxFF potential for Pd/O and application to palladium oxide formation," *Journal of Chemical Physics*, vol. 139, no. 4, p. 044109, 2013.

[33] S. Plimpton, "Fast Parallel Algorithms for Short-Range Molecular Dynamics," *Journal of Computational Physics*, vol. 117, no. 1, pp. 1–19, 1995.

[34] G. J. Martyna, M. L. Klein, and M. Tuckerman, "Nose–Hoover chains: The canonical ensemble via continuous dynamics," *J. Chem. Phys.*, vol. 97, no. 1992, pp. 2635–2643, 1992.

[35] T. Verstraelen, P. W. Ayers, V. Van Speybroeck, and M. Waroquier, "ACKS2: Atom-condensed Kohn-Sham DFT approximated to second order," *Journal of Chemical Physics*, vol. 138, no. 7, 2013.

[36] I. Michio, "Structure and Texture of Carbon Materials," *Carbons for Electrochemical Energy Storage and Conversion Systems*, pp. 37–76, 2009.

[37] P. J. F. Harris, "Structure of non-graphitising carbons," *International Materials Reviews*, vol. 42, no. 5, pp. 206–218, 1997.

[38] P. J. F. Harris, "New Perspectives on the Structure of Graphitic Carbons," *Critical Reviews in Solid State and Materials Sciences*, vol. 30, no. 4, pp. 235–253, 2005.

[39] S. Y. Hong, Y. Kim, Y. Park, A. Choi, N.-S. Choi, and K. T. Lee, "Charge carriers in rechargeable batteries: Na ions vs. Li ions," *Energy & Environmental Science*, vol. 6, no. 7, pp. 2067–2081, 2013.

[40] R. Ramachandran, S.-M. Chen, and G. Peter Gnana Kumar, "Recent Developments in Electrode Materials for Oxygen Reduction Reaction," *Int. J. Electrochem. Sci*, vol. 10, pp. 8581–8606, 2015.

[41] S. P. Ong, V. L. Chevrier, G. Hautier, A. Jain, C. Moore, S. Kim, X. Ma, and G. Ceder, "Voltage, stability and diffusion barrier differences between sodium-ion and lithium-ion intercalation materials," *Energy & Environmental Science*, vol. 4, no. 9, p. 3680, 2011.

[42] P. Ge and M. Fouletier, "ELECTROCHEMICAL INTERCALATION OF SODIUM IN GRAPHITE Pascal GE and Mireille FOULETIER," *Solid State Ionics*, vol. 28-30, pp. 1172–1175, 1988.

[43] M. M. Doeff, M. M. Doeff, Y. Ma, Y. Ma, S. J. Visco, S. J. Visco, L. C. D. Jonghe, and L. C. D. Jonghe, "Electrochemical insertion of sodium into carbon," *Journal of The Electrochemical Society*, vol. 140, no. 12, pp. 169–170, 1993.

[44] Y. Okamoto, "Density Functional Theory Calculations of Alkali Metal (Li, Na, and K) Graphite Intercalation Compounds," *The Journal of Physical Chemistry C*, vol. 118(1), pp. 16–19, 2014.

[45] W. Luo, Z. Jian, Z. Xing, W. Wang, C. Bommier, M. M. Lerner, and X. Ji, "Electrochemically Expandable Soft Carbon as Anodes for Na-Ion Batteries," *ACS Central Science*, vol. 1, pp. 516–522, 2015.

[46] D. A. Stevens and J. R. Dahn, "High Capacity Anode Materials for Rechargeable Sodium-Ion Batteries," *Journal of The Electrochemical Society*, vol. 147, no. 4, p. 1271, 2000.

[47] N. Yabuuchi, K. Kubota, M. Dahbi, and S. Komaba, "Research Development on Sodium-Ion Batteries," *Chemical Reviews*, vol. 114, no. 23, pp. 11636–11682, 2014.

[48] D. A. Stevens and J. R. Dahn, "The Mechanisms of Lithium and Sodium Insertion in Carbon Materials," *Journal of The Electrochemical Society*, vol. 148, no. 8, pp. A803–A811, 2001.

[49] T. Ramireddy, M. M. Rahman, N. Sharma, A. M. Glushenkov, and Y. Chen, "Carbon coated Na7Fe7(PO4) 6F3: A novel intercalation cathode for sodium-ion batteries," *Journal of Power Sources*, vol. 271, pp. 497–503, 2014.

[50] F. Legrain, O. I. Malyi, and S. Manzhos, "Comparative computational study of the energetics of Li, Na, and Mg storage in amorphous and crystalline silicon," *Computational Materials Science*, vol. 94, no. C, pp. 214–217, 2014.

[51] S. C. Jung, D. S. Jung, J. W. Choi, and Y. K. Han, "Atom-level understanding of the sodiation process in silicon anode material," *Journal of Physical Chemistry Letters*, vol. 5, no. 7, pp. 1283–1288, 2014.

[52] R. Ranganathan, S. Rokkam, T. Desai, and P. Keblinski, "Generation of amorphous carbon models using liquid quench method: A reactive molecular dynamics study," *Carbon*, vol. 113, pp. 87–99, 2017.

[53] S. Le Roux and V. Petkov, "{\it ISAACS} {–} interactive structure analysis of amorphous and crystalline systems," *Journal of Applied Crystallography*, vol. 43, pp. 181–185, feb 2010.

[54] K. Chenoweth, A. C. T. van Duin, and W. A. Goddard III, "ReaxFF reactive force field for molecular dynamics simulations of hydrocarbon oxidation," *The Journal of Physical Chemistry A*, vol. 112, no. 5, pp. 1040–1053, 2008.

Appendix A

ReaxFF potential functions

This appendix describes the ReaxFF energy functions in details based on [54].

The total system energy of ReaxFF is constructed by the partial energy contributions given as

$$E_{system} = E_{bond} + E_{over} + E_{under} + E_{vdWaals} + E_{Coulomb} \tag{A.1}$$

ReaxFF determines the connectivity of a molecule by bond order BO'_{ij} obtained directly from the interatomic distance r_{ij}. The total bond order includes contributions from sigma bonds, pi-bonds and double pi-bonds:

$$\begin{aligned} BO'_{ij} &= BO^{\sigma}_{ij} + BO^{\pi}_{ij} + BO^{\pi\pi}_{ij} \\ &= exp\left[p_{bo,1} \cdot \left(\frac{r_{ij}}{r^{\sigma}_0}\right)^{p_{bo,2}}\right] + exp\left[p_{bo,3} \cdot \left(\frac{r_{ij}}{r^{\pi}_0}\right)^{p_{bo,4}}\right] + exp\left[p_{bo,5} \cdot \left(\frac{r_{ij}}{r^{\pi\pi}_0}\right)^{p_{bo,6}}\right] \end{aligned} \tag{A.2}$$

The initial bond orders calculated in Eq. A.2 are overestimated due to weak bonding interactions with neighbor atoms in the molecule. From these uncorrected bond orders, an overcoordination $\Delta^{'}_i$ can be calculated for each atom as the difference between the total bond order around the atom and the number of its bonding electrons Val

$$\Delta'_i = -Val_i + \sum_{j=1}^{n} BO'_{ij} \tag{A.3}$$

For atoms having lone pair of electrons, a softer overcoordination $\Delta^{'boc}_i$ is employed.

$$\Delta^{'boc}_i = -Val^{boc}_i + \sum_{j=1}^{n} BO'_{ij} \tag{A.4}$$

ReaxFF applies uncorrected overcoordinations in the following calculation scheme to correct the bond orders

and remove unrealistic weak bonds .

$$\begin{aligned} BO_{ij}^{\sigma} &= BO_{ij}^{'\sigma} \cdot f_1(\Delta_i^{'}, \Delta'_j) \cdot f_4(\Delta_i^{'}, BO_{ij}^{'}) \cdot f_5(\Delta_j^{'}, BO_{ij}^{'}) \\ BO_{ij}^{\pi} &= BO_{ij}^{'\pi} \cdot f_1(\Delta_i^{'}, \Delta_j^{'}) \cdot f_1(\Delta_i^{'}, \Delta_j^{'}) \cdot f_4(\Delta_i^{'}, BO_{ij}^{'}) \cdot f_5(\Delta_j^{'}, BO_{ij}^{'}) \\ BO_{ij}^{\pi\pi} &= BO_{ij}^{'\pi\pi} \cdot f_1(\Delta_i^{'}, \Delta_j^{'}) \cdot f_1(\Delta_i^{'}, \Delta_j^{'}) \cdot f_4(\Delta_i^{'}, BO_{ij}^{'}) \cdot f_5(\Delta_j^{'}, BO_{ij}^{'}) \\ BO_{ij} &= BO_{ij}^{\sigma} + BO_{ij}^{\pi} + BO_{ij}^{\pi\pi} \end{aligned} \tag{A.5}$$

$$f_1(\Delta_i, \Delta_j) = \frac{1}{2} \cdot \left(\frac{Val_i + f_2(\Delta_i^{'}, \Delta_j^{'})}{Val_i + f_2(\Delta_i^{'}, \Delta'_j) + f_3(\Delta_i^{'}, \Delta_j^{'})} + \frac{Val_j + f_2(\Delta_i^{'}, \Delta_j^{'})}{Val_j + f_2(\Delta_i^{'}, \Delta'_j) + f_3(\Delta_i^{'}, \Delta_j^{'})} \right) \tag{A.6}$$

$$f_2(\Delta'_i, \Delta'_i) = exp(-p_{boc1} \cdot \Delta'_i) + exp(-p_{boc1} \cdot \Delta'_j) \tag{A.7}$$

$$f_3(\Delta_i^{'}, \Delta_j^{'}) = -\frac{1}{p_{boc2}} \cdot ln \left\{ \frac{1}{2} \cdot \left[exp(-p_{boc2} \cdot \Delta_i^{'}) + exp(-p_{boc2} \cdot \Delta_j^{'}) \right] \right\} \tag{A.8}$$

$$f_4(\Delta'_i, BO_i^{'}j) = \frac{1}{1 + exp(-p_{boc3} \cdot (p_{boc4} \cdot BO_{ij}^{'} \cdot BO_{ij}^{'} - \Delta_i^{'boc}) + p_{boc5})} \tag{A.9}$$

$$f_5(\Delta'_j, BO_i^{'}j) = \frac{1}{1 + exp(-p_{boc3} \cdot (p_{boc4} \cdot BO_{ij}^{'} \cdot BO_{ij}^{'} - \Delta_)^{'boc} + p_{boc5})} \tag{A.10}$$

By using the correct bond order obtained, the corrected overcoordination Δ_i can then be calculated. If $\Delta_i > 0$ the atom is overcoordinated, and if $\Delta_i < 0$, it is undercoordinated and must be further corrected.

$$\Delta_i = -Val_i + \sum_{j=1}^{n} BO_{ij} \tag{A.11}$$

The first energy term E_{bond} can then be calculated with the correct bond orders

$$E_{bond} = -D_e^{\sigma} \cdot BO_{ij}^{\sigma} \cdot exp\left[p_{be1}(1 - (BO_{ij}^{\sigma})^{p_{be2}}\right] - D_e^{\pi} \cdot BO_{ij}^{\pi} - D_e^{\pi\pi} \cdot BO_{ij}^{\pi\pi} \tag{A.12}$$

Even though bond order correction does remove overcoordination in the molecule, some degree may still remain. E_{over} is imposed to correct overcoordinated atoms.

$$E_{over} = \frac{\sum_{j=1}^{nbond} p_{ovun1} \cdot D_e^{\sigma} \cdot BO_{ij}}{\Delta_i^{lpcoor} + Val_i} \cdot \Delta_i^{lpcorr} \left[\frac{1}{1 + exp(p_{ovun2} \cdot \Delta_i^{lpcorr})} \right] \tag{A.13}$$

$$\Delta_i^{lpcorr} = \Delta_i - \frac{\Delta_i^{lp}}{1 + p_{ovun3} \cdot exp\left(p_{ovun4} \cdot \{\sum_{j=1}^{neighb(i)} (\Delta_j - \Delta_j^{lp}) \cdot (BO_{ij}^{\pi} + BO_{ij}^{\pi})\}\right)} \tag{A.14}$$

In contrast, for an undercoordinated atom ($\Delta_i < 0$), energy contribution from π-electron system is taken to account. Thus, E_{under} is especially important in cases where the undercoordinated atom i and its under-

coordinated neighbors j have partly π-bond character.

$$E_{under} = -p_{ovun5} \cdot \frac{1 - exp(p_{ovun6} \cdot \Delta_i^{lpcor})}{1 + exp(-p_{ovun2} \cdot \Delta_i^{lpcor})} \cdot \frac{1}{1 + p_{ovun7} \cdot exp\left[\sum_{j=1}^{nei(i)} (\Delta_j - \Delta_j^{lp})(BO_{ij}^{\pi} + BO_{ij}^{\pi\pi})\right]} \quad \text{(A.15)}$$

ReaxFF considers non-bonded interactions for all atom pairs, regardless of connectivity. To calculate the van der Waals interaction term, a distance-corrected Morse potential is used. The energy expression contains a shielding term γ_{ij}^{cdW} such that excessive repulsion at short distances is avoided.

$$E_{vdW} = Tap \cdot E_{ij}^{vdW} \cdot \left\{ exp\left[\alpha \cdot \left(1 - \frac{f_{13}(r_{ij})}{r_{vdW}}\right)\right] - 2 \cdot exp\left\{\frac{1}{2} \cdot \alpha_{ij} \cdot \left(1 - \frac{f_{13}(r_{ij})}{r_{ij}^{vdW}}\right)\right]\right\} \quad \text{(A.16)}$$

$$f_{13}(r_{ij}) = \left[r_{ij}^{p_{vdW1}} + \left(\frac{1}{\gamma_{ij}^{vdW}}\right)^{\frac{1}{p_{vdW1}}}\right]^{\frac{1}{p_{vdW1}}} \quad \text{(A.17)}$$

Similar to the van der Waals interaction, the Coulomb energy term is also shielded. Atomic charges q_i and q_j are calculated using either the EEM-approach or the QEq-scheme.

$$E_{Coulomb} = Tap \cdot C \cdot \frac{q_i \cdot q_j}{\left[r_{ij}^3 + \left(\frac{1}{\gamma_{ij}}\right)^3\right]^{\frac{1}{3}}} \quad \text{(A.18)}$$

To ensure a smooth cut-off in non-bonded energy terms, ReaxFF employs a Taper correction, which scales to a 7th order polynomial

$$Tap = Tap_7 \cdot r_{ij}^7 + Tap_6 \cdot r_{ij}^6 + Tap_5 \cdot r_{ij}^5 + Tap_4 \cdot r_{ij}^4 + Tap_3 \cdot r_{ij}^3 + Tap_2 \cdot r_{ij}^2 + Tap_1 \cdot r_{ij} + Tap_0 \quad \text{(A.19)}$$

The Tap-terms ensure at that each derivatives of the non-bonded interactions are continous and and go to smoothly to zero at the cut-off distance. The Tap-terms are determined from the non-bonded cut-off radius R_{cut}

$$\begin{aligned} Tap_7 &= 20/R_{cut}^7 \\ Tap_6 &= -70/R_{cut}^6 \\ Tap_5 &= 84/R_{cut}^5 \\ Tap_4 &= -35/R_{cut}^4 \\ Tap_3 &= 0 \\ Tap_2 &= 0 \\ Tap_1 &= 0 \\ Tap_0 &= 1 \end{aligned} \quad \text{(A.20)}$$

Appendix B

LAMMPS input

The LAMMPS input for the liquid-quenching steps for creating amorphous carbon models.

```
#LAMMPS INPUT SCRIPT

#------------------ Initialize Simulation ------------------
clear
units real
dimension 3
boundary p p p
atom_style charge
atom_modify map array
#--------------- Define simulation box -----------------
variable nrC equal 125
region box block 0.0 10 0.0 10 0.0 10
create_box 1 box
create_atoms 1 random $(v_nrC) 8321981 box
mass 1 12.00
set type 1 charge 0
#------------------------ Define FF --------------------------
pair_style reax/c NULL safezone 1.5 mincap 100
pair_coeff * * ffield.reax C
neighbor 2.0 bin
#---------------------- Define settings ----------------------
compute peratom all pe/atom
compute_modify peratom dynamic yes
dump 1 all xyz 1000 amorp_C2.xyz
dump_modify 1 element C append yes

reset_timestep 0
timestep 0.01
restart 200000 restart
#------------------ Equilibration -----------------
thermo 1000
thermo_style custom step temp atoms press pe etotal temp density vol
fix 1 all qeq/reax 1 0.0 10.0 1.0e-6 reax/c
fix 2 all nvt temp 10000.0 10000.0 1000.0
run 1000000

fix 3 all nvt temp 10000.0 3000.0 100.0
run 2000000

fix 3 all nvt temp 3000.0 3000.0 1000.0
run 1000000

fix 4 all nvt temp 3000.0 300.0 100.0
run 2000000

fix 5 all nvt temp 300.0 300.0 1000.0
run 1000000
write_data data.2.5_lq1
print "All done!"
```